Chapter-6

Phosphorylation of rice straw for production of heat-sealable packaging films and thermal box

Motivation

Agricultural biomass such as rice straws represent a significant volume of waste generated worldwide; disposal of which through landfilling and burning is a major global challenge. In present study, strategic functionalization of rice straws through delignification-cum-phosphorylation using low-cost agro-chemicals followed by scalable processing into films beverage cups and thermal boxes are developed.

Key Highlights:

- ***Utilisation of Rice Straw Waste:*** *The chapter addresses environmental concerns related to rice straw waste by utilising them as a source for cellulose extraction to produce phosphorylated gels, a sustainable alternative to conventional disposal methods.*
- ***Alternative to Plastic Packaging:*** *The proposed valorization of rice straws into packaging films and beverage cups with lower ecological impacts and commercial feasibility provides a sustainable alternative for a promising plastic-free world.*
- ***Transformation into Packaging Foam:*** *This chapter presents a sustainable alternative to the environmentally harmful polystyrene foam by transforming phosphorylated gels into packaging foam.*

The work in this chapter is under preparation as:

1. *Rahul Ranjan, Vedang P. Mone, Rohit Rai, Chandra Kant and Prodyut Dhar, Biomass-derived all-cellulose phosphate-based heat sealable films and thermally stable anti-fizzing cups with improved recyclability.* ***(Chemical Engineering Journal, Under review)***
2. *Rahul Ranjan and Prodyut Dhar, Sustainable cellulose-silica aerogels with low thermal conductivity and flame-retardant properties for packaging of perishable food products (**To be submitted**)*

Graphical Abstract

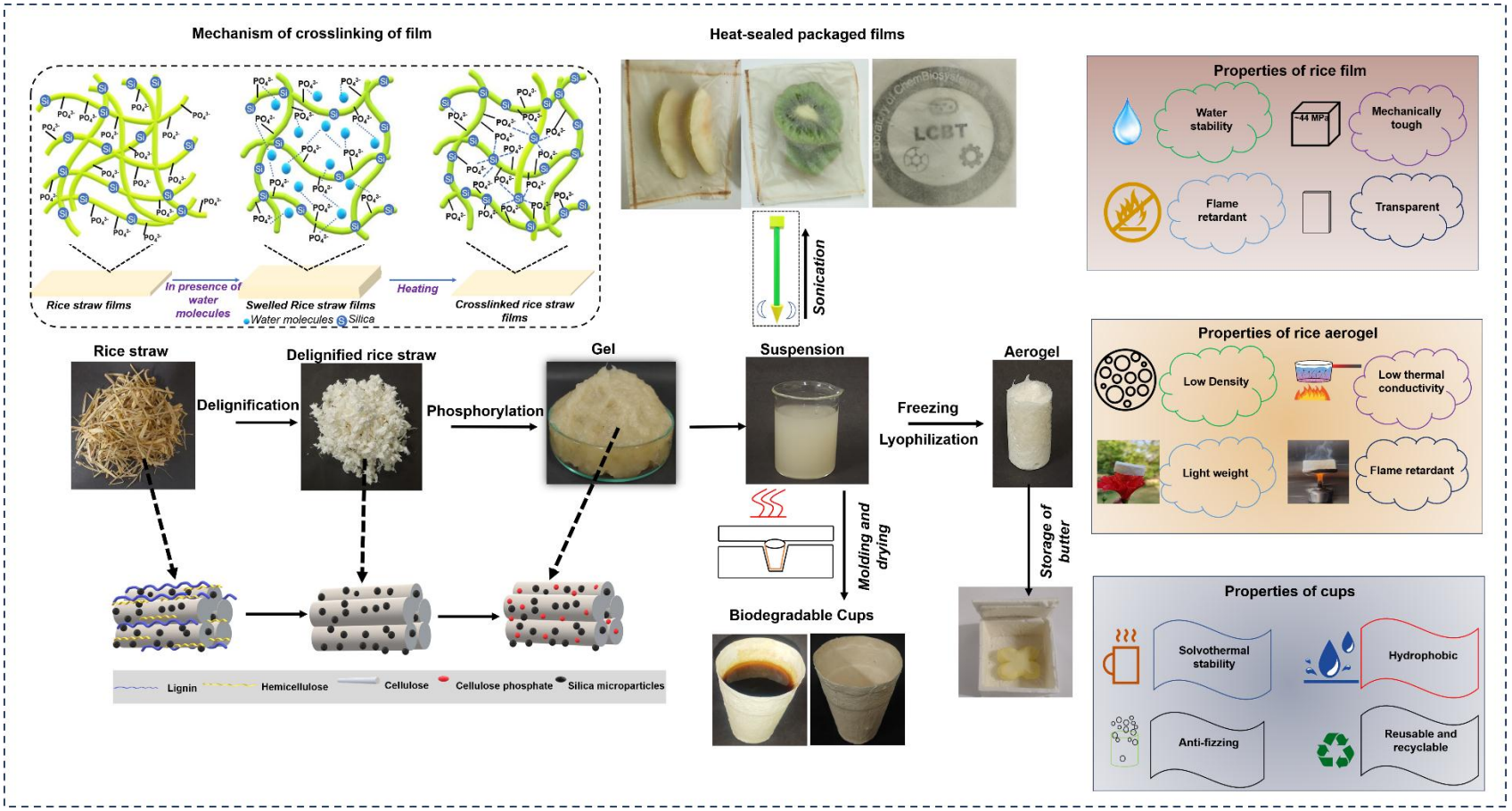

6.1 Introduction

The excessive consumption of plastic packaging due to its easy availability, processability, low cost, durability and strength has posed an imminent threat to aquatic and terrestrial ecosystems. In the last two decades, 460 million tons of plastic have been produced worldwide, contributing to 3.4% of all greenhouse gas emissions with issues related to their disposal and microplastic pollution [557,558]. Moreover, disposal of agricultural residues post-harvest through land-filling or burning has been one of the major global concerns as it generates emissions of hazardous gaseous pollutants [559]. Among different crops harvested, rice harvesting generates a variety of waste by-products such as straw, husk, ash, and bran with each kg of rice production generating almost 1.5 kg of waste rice straws [560]. Rice is grown globally, with China and India generating more than 60% of the world's rice production; therefore, surplus amounts of rice waste are abundantly available for utilization [560]. To reduce global plastic consumption and overcome its ecotoxicological effects, the development of eco-friendly, biodegradable, and sustainable alternatives using abundantly available agro-waste biomass such as rice straws is need of the hour. Rice straw is a lignocellulosic complex composed of cellulose (38%), hemicellulose (27.7%), lignin (13%), and ashes (~15%) [561]. Due to its interesting physiochemical and structural properties, biodegradability and abundance, it has been used for various applications such as developing filler materials, electronic and sensor devices for food packaging [562], wastewater treatment [563], supercapacitor [564], and construction [565]. Delignified rice straw (DRS) consists of cellulose with free hydroxyl groups that can be easily subjected to chemical modification *via* TEMPO-oxidation, acetylation, carboxymethylation, phosphorylation, nitration, and periodate oxidation [566].

Extracting cellulose or cellulose-based fillers from renewable resources is widely studied to develop food packaging materials [567]. Arun et al. extracted cellulose from coconut coir *via* acid hydrolysis-*cum*-bleaching to develop polyvinyl alcohol-based composites with free radical scavenging ability, improved hydrophobicity (91.3°), and tensile strength [568]. In another study, Perumal et al. extracted cellulose nanocrystals (CNC) from rice straw to prepare chitosan/polyvinyl alcohol-based composites with high tensile strength ~ 98 MPa, transparency ~80%, and degradation of ~ 70% in 60 days [569]. Similar studies on using rice straws as nano/micro fillers or for cellulose extraction have been extensively studied [570–574].

Aerogels are solid three-dimensional materials that are highly porous with upto 99% porosity. They are generated from organic (carbon material, polyaniline, resorcinol–formaldehyde), inorganic (silica), or hybrid precursors using methods such as sol-gel or specific drying techniques such as supercritical CO_2 drying, freeze drying, microwave drying, and ambient pressure drying [575]. Furthermore, aerogels are light material with low density (0.015–0.1 g/cm^{-3}) [576], high surface area (10–975 m^2 g^{-1}) [577], low thermal conductivity (0.018 to 0.075 W m^{-1} K^{-1}) [577] and excellent compressibility. Among all the aerogel precursors, lignocellulosic biomass such as rice straw [578], pineapple leaf [577], waste cotton residues [577], coir fibres, Neptune grass [579], sugarcane bagasse [580] have gotten much attention due to their biodegradable, and renewable attributes. These aerogels were studied for different applications such as the preservation of meat [576], cheese [316], beef [581], oil-water separation [582], solar evaporation [583], acoustic insulation [584], thermal insulation [577], an anodic component of battery [585].

This chapter presents a novel method for utilising rice straw by converting it into sustainable packaging materials and high-performance aerogels while adhering to environmentally sustainable practices. By employing an effective phosphorylation technique with inexpensive agrochemicals, we transform rice straw into cellulose phosphate gels, providing a more environmentally friendly option than conventional TEMPO oxidation procedures. LCA studies are performed to examine the environmental impact of our phosphorylated cellulose gel production process in comparison to traditional approaches. We created packaging films and cups made from cellulose, designed to be stable in solvothermal conditions. These products are made using functionalized gels and can be produced on a large scale utilising an efficient processing method. An in-depth investigation is conducted on functionalizing cellulose phosphate gel and its diverse CC. The packaging films from phosphorylated RS have inherent heat-sealing properties and are water-resistant without requiring extra additives. This offers a viable alternative to wax coatings or adhesives typically employed in conventional food packaging. In addition, our moulded cups exhibit enhanced structural and solvothermal stability when exposed to high temperatures, thereby resolving problems related to microplastics in traditional paper or plastic cups used for hot drinks. We present a simple and precise technique for creating lightweight and porous aerogels to further develop our environmentally friendly procedures. These aerogels can absorb large amounts of water and possess low heat conductivity. We highlight the practical implementation of these aerogels by employing them in the butter packaging. The aerogel efficiently retains butter at ambient temperature, ensuring its structural integrity without undergoing melting or distortion for up to six hours. Furthermore, it increases the duration that butter may be stored without spoilage by

inhibiting the proliferation of harmful microorganisms for seven days, whether in cold or room temperatures. Our state-of-the-art food storage system enhances product preservation and reduces carbon emissions in refrigeration, transportation, and cold storage. By employing a newly developed cellulose-silica composite aerogel box, we have effectively devised a packaging remedy that is both ecologically sustainable and environmentally benign. This chapter has been divided into two subsections**. Section 6.2** discusses the application of rice straw films as packaging material for fruits. Further, **section 6.3** focuses on the application of rice straw aerogels for packaging butter.

6.2 Results and discussion

The rice straws were strategically modified to produce transparent, heat-sealable, flexible packaging films and hydrostable beverage cups with improved mechanical strength, flame retardancy and environmental sustainability. Delignification-*cum*-phosphorylation approach was optimized at different curing times to produce gels with high CC, which shows the transition from transparent to pale brown (***Figure 6.1***). The gels were casted into films and molded into cups with their ability to withstand hot beverages and preserve perishable fruits improving their shelf-life. The mechanism for grafting of phosphate groups on cellulose backbone and silicon phosphate cross-linkages upon heating were studied through XPS and FTIR studies. Interestingly, all-cellulose-based films were found to be heat-sealable without any additives and evaluated for migration properties in the presence of various food simulants. The cups were assessed for solvothermal stability, anti-fizzing and surface wettability, which led to improved washability and reusability for at least three times. To understand the environmental impacts generated, LCA studies were carried out for

the proposed process and compared with traditional TEMPO oxidation for commercial cellulose film production.

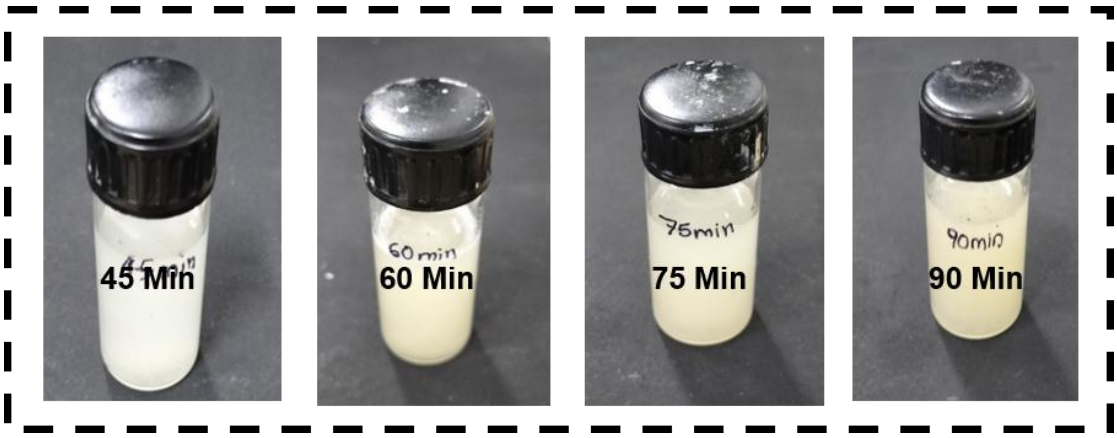

Figure 6.1 *Effects of curing duration on the colour of the produced phosphorylated RS gels.*

6.2.1 Physiochemical properties of RS films

The CC of films were determined from conductometric titration curve, as shown in ***Figure 6.2***, which shows three distinct regions. The first region is highly acidic, resulting in a large consumption of H^+ ions, causing an overall decrease in the suspension's conductivity on titration with NaOH. In the second region, a neutralization reaction occurs with the acidic groups available on the surface of cellulose, resulting in a plateau region. In the last region, the suspension's pH increases due to the excess addition of NaOH, leading to a sharp increase in the conductivity. ***Figure 6.2*****(a),** ***Figure 6.2*****(b),** ***Figure 6.2*****(c),** and ***Figure 6.2*****(d)** corresponds to the conductometric titration curve for RSF-45, RSF-60, RSF-75, and RSF-90, respectively, clearly shows the appearance of only one inflection point confirming the titration of the single free hydroxyl group of cellulose [15]. The RSF-90 film exhibited a maximum charge of 2366 mmol kg^{-1}, while RSF-45, RSF-60, and RSF-75 showed CC of 1850, 2033, and 1616 mmol $kg^{-1,}$ respectively. An increase in the CC of films with increased curing time

was observed due to the swelling of cellulose in the presence of urea, which led to improved infiltration of phosphate ions during phosphorylation [225]. It is expected that the presence of silica in phosphorylated rice straw also improved the thermal stability of fibres, preventing its degradation and improving CC. The curing temperature was optimized at 150 °C, showing minimal degradation of fibres and hydrolysis of pre-existing phosphate diester bond in DAP required for an overall increase in CC [193],[586].

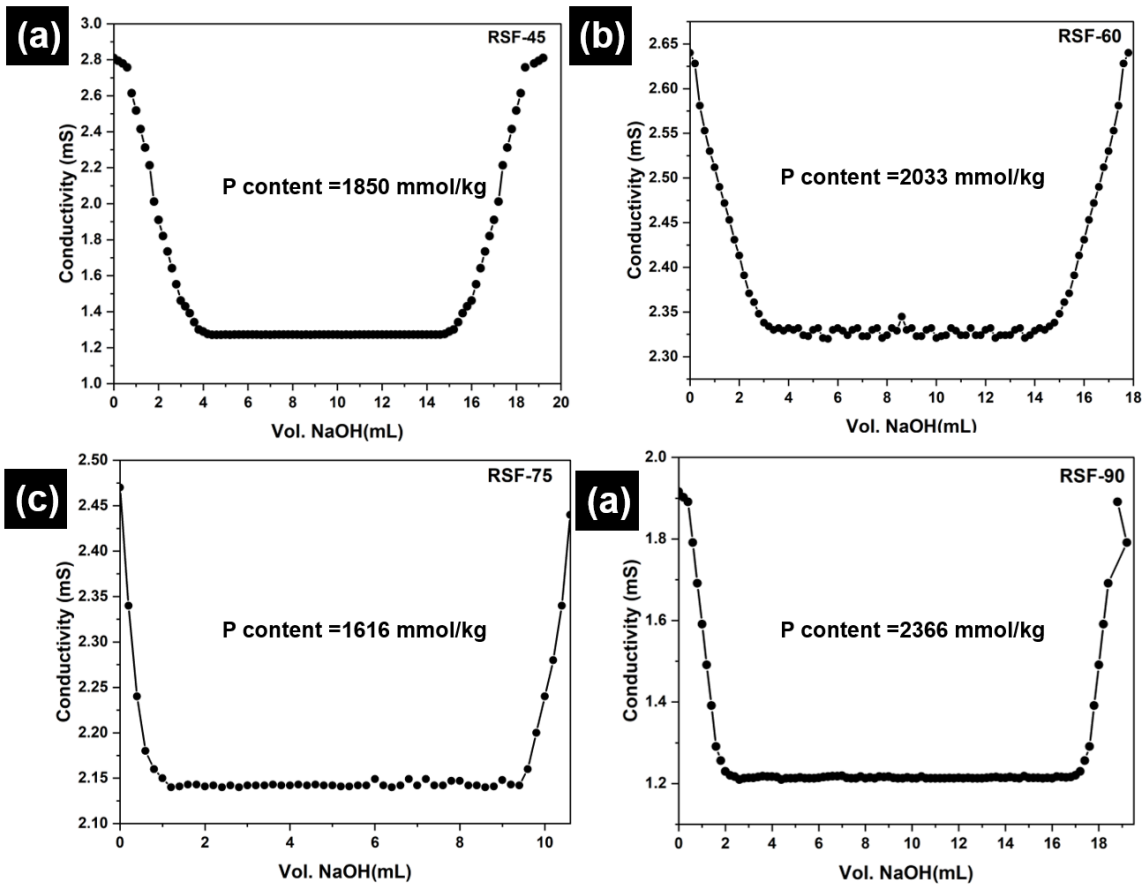

Figure 6.2 *Phosphate content of the films produced after different curing times measured using conductometric titration.*

6.2.2 LCA for production of phosphorylated RSF films and its comparison with TEMPO-oxidized films

The environmental impacts generated during the production of phosphorylated RSF films and TEMPO-oxidized films are compared in ***Figure 6.3***. TEMPO-oxidation is one of the most widely used chemical modification techniques for producing functionalized cellulose with excellent film-forming ability and improved physiochemical, structural, mechanical and thermal properties. ***Figure 6.3*****(a-c)** shows that both routes show slight differences in impact values generated in different environmental categories during film production. For the production of phosphorylated RSF film, climate change showed the highest impact in including and excluding the biogenic carbon category ~13.5 kg CO_2 eq. However, producing TEMPO-oxidized films from Eucalyptus pulp generated almost similar impact ~11.3-11.7 kg CO_2 eq. in including and excluding biogenic carbon categories. The impact generated in the human toxicity non-cancerous category was lower for phosphorylated RSF films, 0.137 kg 1,4-DB eq compared to 0.146 kg 1,4-DB eq. for TEMPO-oxidation films. The impacts generated in the photochemical ozone formation (environment) category for RSF and TEMPO-oxidation films production were 0.0157 and 0.0138 kg NO_x eq. respectively. The impact generated in the terrestrial ecotoxicity category was 0.875 kg 1,4-DB eq. for RSF film and 0.807 kg 1,4-DB eq. from TEMPO-oxidation film. In fossil depletion, the impacts were ~3.05 and 2.67 kg oil eq. from RSF and TEMPO-oxidized films, respectively. The high impact of the TEMPO-oxidation process in various categories was primarily due to the emissions during electricity (hard coal) consumption and the utilization of various chemicals in high quantities during film production. In fine particulate matter formation, the impact generated was almost similar to ~ 0.0044 and

0.0038 kg PM 2.5 eq. in both routes. It was observed that the RSF film production *via* the phosphorylation route shows lowered environmental impacts in freshwater consumption, metal depletion, freshwater ecotoxicity, stratospheric ozone depletion, ionizing radiation, and freshwater and marine eutrophication categories. Therefore, the proposed route for phosphorylated RSF film production using agro-based chemicals is a cost-effective and scalable technology alongwith an environmentally friendly and sustainable process.

6.2.2.1 Normalization of mid-point results of production of phosphorylated RSF and TEMPO-oxidised films

From ***Figure 6.3*****(d-e)**, it was observed that for both production processes, three out of total eighteen impact categories had the most significant influence on overall LCA parameters. These categories were climate change (excluding biogenic carbon), fossil depletion, and photochemical ozone formation (ecosystems). Among these categories, the highest impact was observed for the fossil depletion category, with 0.0027 kg oil eq. and 0.0031 kg oil eq. for TEMPO-oxidation and RSF film production, respectively. The climate change category (excluding biogenic carbon) had the second highest impact of 0.0014 kg CO_2 eq. and 0.0016 kg CO_2 eq for TEMPO-oxidation and RSF film production, respectively. For photochemical ozone formation (ecosystems) impacts were almost similar~ 0.0007 kg NO_x eq. and 0.0008 kg NO_x eq. for both film production routes. The normalization mid-point results indicate that climate change (excluding biogenic carbon), fossil depletion, and photochemical ozone formation (ecosystems) dominated the overall environmental impact and, hence, were chosen for sensitivity analysis, as discussed in the subsequent section.

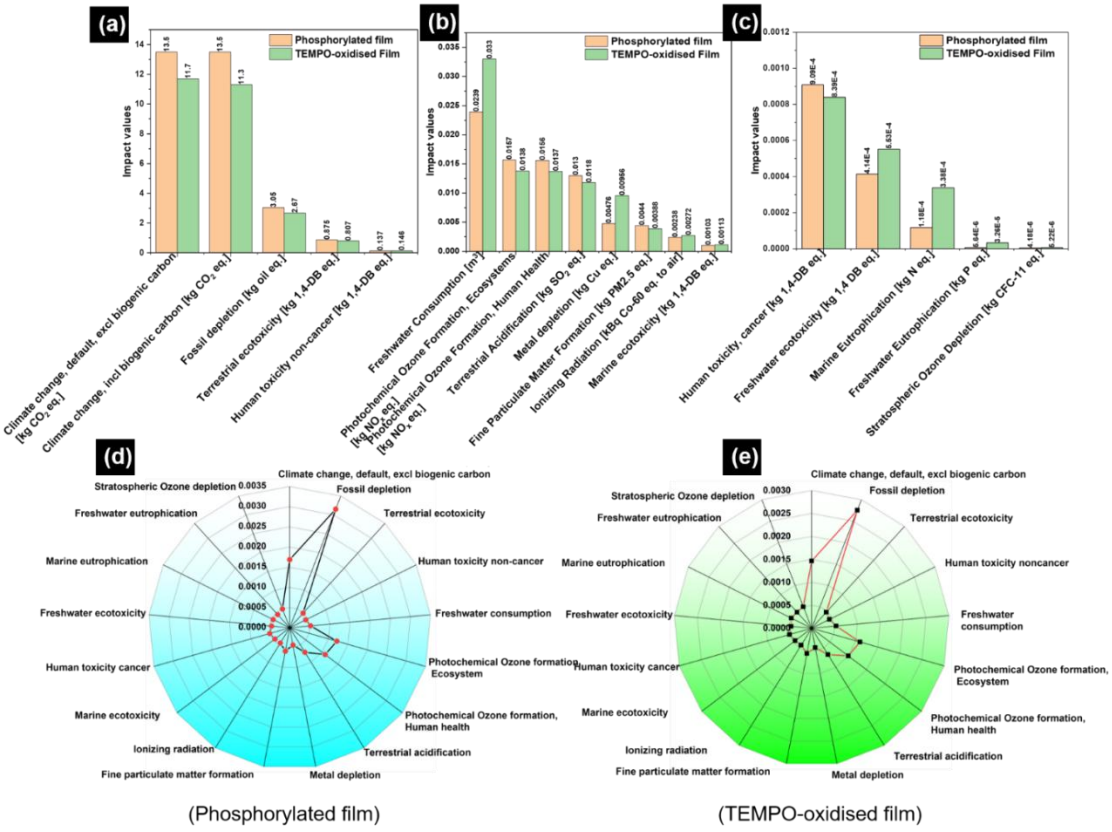

Figure 6.3 *(a-c) Represent the environmental impact generated during the production of nanocellulose via TEMPO-oxidation routes and phosphorylation routes, radar graph for the production of functionalized cellulose films via (d) phosphorylation film production route and (e) TEMPO-oxidation film production route.*

6.2.2.2 Sensitivity analysis for production of phosphorylated RSF and TEMPO-oxidised films

As shown in ***Table 6.1***, sensitivity analysis was performed for critical parameters such as electricity, delignification, and phosphorylation processes by increasing and decreasing the parameters by 10% and 8%, respectively. The effect on three critical dominating impact categories, such as climate change (excluding biogenic carbon), fossil depletion, and photochemical ozone formation (ecosystems), was evaluated. When electricity supply was increased by 10%, a proportional increase in impacts was observed. However, the highest relative increase was recorded in the photochemical ozone formation category, which was 12.79%. On the other hand, when

the electricity supply was decreased by 8%, the most significant reduction in the climate change category was observed at −8.1%. Additionally, the fossil depletion category observed a significant decrease of 7.86%. The delignification process resulted in 7.33% increase in impact for photochemical ozone formation category when there was a 10% increase. Similarly, a notable increase of 8.66% and a decrease of −3.84% were observed in photochemical ozone formation category when there was a 10% increase and 8% decrease, respectively, in phosphorylation process. The sensitivity analysis highlights that electricity consumption as predominant parameter which exhibits proportional increment or decrement corresponding to different levels throughout the production process.

Table 6.1 *Sensitivity analysis of dominant impact categories obtained from normalization of phosphorylated RSF film for parameters such as electricity, delignification and phosphorylation process.*

Categories	**Electricity**		**Delignification**		**Phosphorylation**	
	10% increase	8% decrease	10% increase	8% decrease	10% increase	8% decrease
Climate change	10.37	-8.1	2.96	-5.92	3.7	-2.96
FD	10.16	-7.86	2.62	-7.86	3.6	-3.27
POF	12.79	-6.66	7.33	-2.0	8.66	-3.84

6.2.3 Functional, structural and thermal properties

6.2.3.1 Functional properties RSF

FTIR studies were carried out to understand changes in the chemical functionalities of rice straw during delignification, followed by phosphorylation to produce RSF films (***Figure 6.4*****(a))**. The IR-peaks at 1320 cm^{-1}, 1628 cm^{-1}, 1160 cm^{-1}, 2929 $cm^{-1,}$ and 3350 cm^{-1} present in all samples corresponds to cellulose backbone,

which represents -CH_2 bending, -OH vibration, -CH_2 asymmetric vibration due to presence of glycosidic bonds, -CH and -OH stretching respectively [15,587,588]. Due to the inherent presence of silica in rice, the FTIR spectrum for all samples shows peaks at 795 cm^{-1}, 1036 cm^{-1}, and 1063 cm^{-1}, corresponding to Si-O-Si asymmetric stretching [589–591]. The phosphorylation was confirmed from peaks at 815 cm^{-1} and 917 cm^{-1}, corresponding to P-O-C and P=O bonds, respectively [592].

6.2.3.2 Structural properties of RSF

XRD diffractograms of RS, DRS, and RSF films produced after the phosphorylation were studied to understand the changes in crystal properties **(*Figure 6.4*(b))**. In RS, two peaks were observed at 16.2° and 22.2°, representing cellulose I with planes (110) and (200), respectively. After delignification, the intensity of the peak at 22.2° increased with the improvement in crystallinity from 47.8% (for RS) to 52.6% (for DRS). There was a shift of ~ 1° in each produced film, namely RSF-45, RSF-60, RSF-75, and RSF-90, compared to RS and DRS (from 22.2° to 21.5°). A new peak emerged at 24.5° in each developed film corresponding to the crystal plane of (002) cellulose [593,594]. The C.I. of films developed were 40.8 %, 44.4 %, 54.7 %, and 27.0 % for RSF-45, RSF-60, RSF-75, and RSF-90 respectively, and the size of the crystallite was 5.5 Å (16.2°), 3.9 Å (22.2°), 4.1 Å (21.5°), and 3.6 Å (24.5°). CI of the film increased with the reaction time of up to 75 min, and it decreased for RSF-90 due to prolonged phosphorylation, which results in the decomposition of the cellulose fibres [17,595]. During the curing process with urea, cellulose dissolution occurs, which might disrupt the inter- and intra-hydrogen bonding structures in the amorphous region, thereby decreasing crystallinity[16,193,596].

6.2.3.3 Thermal properties of RSF

TGA of RS, DRS and phosphorylated films were studied to investigate their thermal properties by measuring the weight change corresponding to applied temperature, as shown in ***Figure 6.4*****(c)** and ***Table 6.2***. The thermal degradation of RS and DRS started at 105 °C with a weight reduction of 3.1% and 3.2%, respectively, due to the removal of trapped moisture. The 10% weight reduction of RS and DRS was observed at 264.9 °C and 161.7 °C respectively. The maximum degradation of 48.1% and 73.2% was observed at 553.2 °C and 368.1 °C for RS and DRS, respectively. The residual weight observed at 700 °C was 18.6% and 11.0% for RS and DRS, respectively. The reduction in thermal stability of RS on delignification is mainly due to the removal of the lignin component and the breakdown of the linkage between cellulose and lignin, which reduced the char formation. Thermal degradation of phosphorylated films RSF-45, RSF-60, RSF-75, and RSF-90 starts at 105 °C with degradation in a 2.3 -5.0% range. The temperature at which 10% weight loss was observed varied for each film with 211.2°C, 211.2 °C, 158.8 °C, and 217.4 °C for RSF-45, RSF-60, RSFF-75, and RSF-90 respectively. The maximum degradation temperature of RSF-45, RSF-60, RSFF-75 and RSF-90 films observed 263.0 °C, 263.0 °C, 195.2 °C, and 249.0 °C respectively with maximum weight loss of 34.6 %, 35.0 %, 28.6 %, and 25.5% respectively. The variation in temperature at which maximum weight loss is observed is mainly due to the difference in the DS of phosphate groups. The earlier degradation observed in films is mainly due to phosphate ions catalytic activity, which initiates the decomposition of the cellulosic backbone, forming low molecular weight monomeric units [15,16]. At 700 °C, percentage char formation was observed to be ~49.0%, 50.0%, ~36.0% and 56.2% for RSF-45, RSF-60, RSF-75 and

RSF-90, respectively, which increased with phosphate CC [16,597]. Additionally, the rise in film residual mass clearly shows that phosphorylation occurred at *C6* with the ceasing of decomposition of cellulosic materials, demonstrating good thermal stability in comparison to unmodified cellulose films, which results in improved flame retardancy as discussed in subsequent sections [15,205].

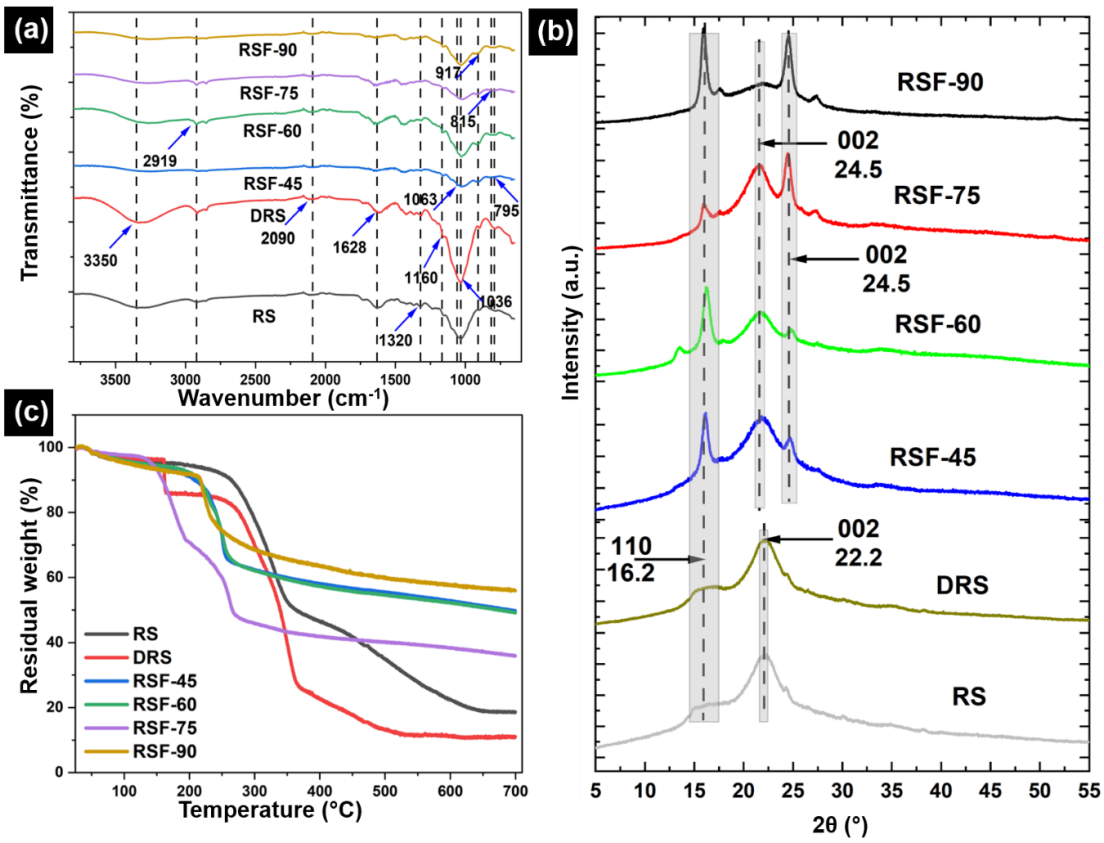

Figure 6.4 *(a) FTIR, (b) TGA, and (c) X-ray diffraction of rice straws, delignified rice straw, and developed RSF films.*

6.2.4 Mechanistic investigation: XPS studies of DRS and RSF-60

XPS analysis of RSF-60 and DRS was conducted to confirm the presence of phosphate groups and mechanistically understand the formation of phosphorylated cellulose. ***Figure 6.5*****(a)** shows the broad scan XPS survey of RSF-60 and DRS, with binding energy at 532.7 eV, 285.7 eV, and 103.6 eV representing characteristic peaks

of *O1s*, *C1s*, and *Si2p*, respectively. The small intensity peak at 134.0 eV corresponds to *P2p*, confirming the formation of covalently-linked phosphate with cellulose backbone in RSF-60. ***Figure 6.5*****(c)** shows the deconvoluted peaks of *C1s* of RSF-60 at 287.2, 284.7, and 286.1 eV representing C=O, C-C/C=C, and C=O bonds respectively [598–600]. The deconvoluted peaks at 288.3, 286.0, and 284.8 eV in *C1s* **(*Figure 6.5*(c))** of DRS represent C=O, C-O-C and C-C bonds, respectively [17,490]. The XPS broad spectrum of *O1s* of RSF-60 (***Figure 6.5*****(a)),** with peaks at 532.6 and 532.0 eV represents P-OH and P=O/P-O/O=C-O=P bonds respectively [601,602]. The deconvoluted peaks of *O1s* **(*Figure 6.5*(e))** at 532.3 and 532.0 eV in broad spectrum of DRS represent C-OH and C=O bonds, respectively [602,603]. ***Figure 6.5*****(d)** in RSF-60 shows broad spectrum deconvoluted peaks for *P2p* at 133.8 and 133.2 eV corresponding to P=O and P-O-C, respectively, [604–606]. The deconvoluted peaks of RSF-60 for *Si2p* **(*Figure 6.5*(b))** at 103.0 and 101.7 eV correspond to Si-P and Si-O-C bond [607,608]. The deconvoluted peaks of *Si2p* at 103.0 and 102.9 eV of DRS **(*Figure 6.5*(b))** represent Si-O and Si-C bonds, respectively [609,610], arising from silica. The presence of P=O, P-O, Si-P, and Si-O-C bonds confirms the formation of covalent linkages of phosphate groups on the cellulose backbone present in rice straw alongwith the bonding of silica with phosphate groups as shown in ***Figure 6.5*****(f-g)**. The presence of covalent linkages between the silica and phosphate groups in films makes them highly stable in water, alongwith with improved mechanical and flame retardancy, as discussed in subsequent sections.

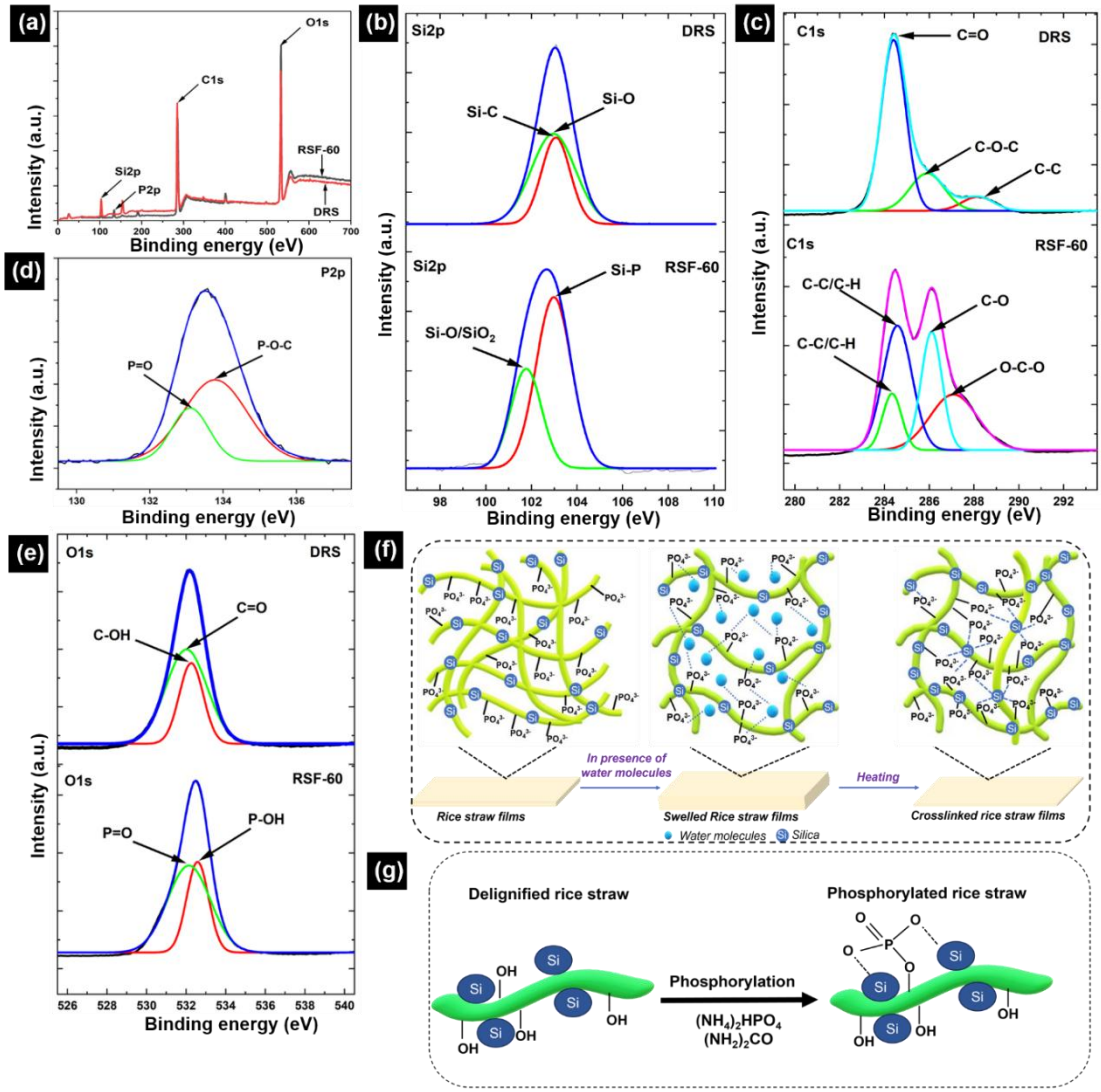

Figure 6.5 *High-resolution XPS spectra of (a)O1s, (b) Si2p, (c) C1s, (d) P2p spectra, (e) broad range XPS spectra of RSF-60 and DRS (f) mechanism of swelling of rice film (g) possible reaction mechanism involved during phosphorylation process.*

Table 6.2 *TGA parameters of rice straws and effect of curing times.*

Samples	T_{onset} **(°C), 10% Degradation**	T_{max} ***(°C) Temperature***	**Weight Reduction (%) at** T_{max}	**Residual Weight (%)**
RS	264.4	354.0	51.7	18.6
DRS	162.8	365.7	27.3	11.0
RSF-45	207.2	262.5	65.91	49.0
RSF-60	212.0	257.4	66.1	49.8
RSF-75	156.2	270.5	48.5	35.9
RSF-90	216.3	244.3	75.1	55.9

6.2.5 Morphological properties of RSF-60

Figure 6.6**(a)** illustrates the morphological characteristics of phosphorylated films, with the intertwined thread-like cellulose fibrils observed in the RSF-60 film. At higher magnification, RSF-60 **(*Figure 6.6*(b))** displays microfiber structures (average diameter ~ 8.2 µm **(*Figure 6.6*(c))** that are entangled and arranged randomly to form network-like structures. On further higher magnification, the film's surface shows white spherical clusters **(*Figure 6.6*(d)** and ***Figure 6.6*(e)),** which could be due to the presence of silica microparticles [611–613] (with average size ~ 2.91 µm) **(*Figure 6.6*(f)**). EDS analysis confirmed the presence of silica particles (at 5.43 wt.%), which are uniformly distributed on the surface of the cellulose fibres as confirmed from the mapping studies (yellow colour represents the Si distribution, ***Figure 6.6*(h)**). The presence of phosphorus (5.34 atomic %) in the EDS spectrum **(*Figure 6.6*(g))** confirms the successful phosphorylation of cellulose, which is distributed uniformly, as evident from elemental mapping of phosphate **(*Figure 6.6*(i))**.

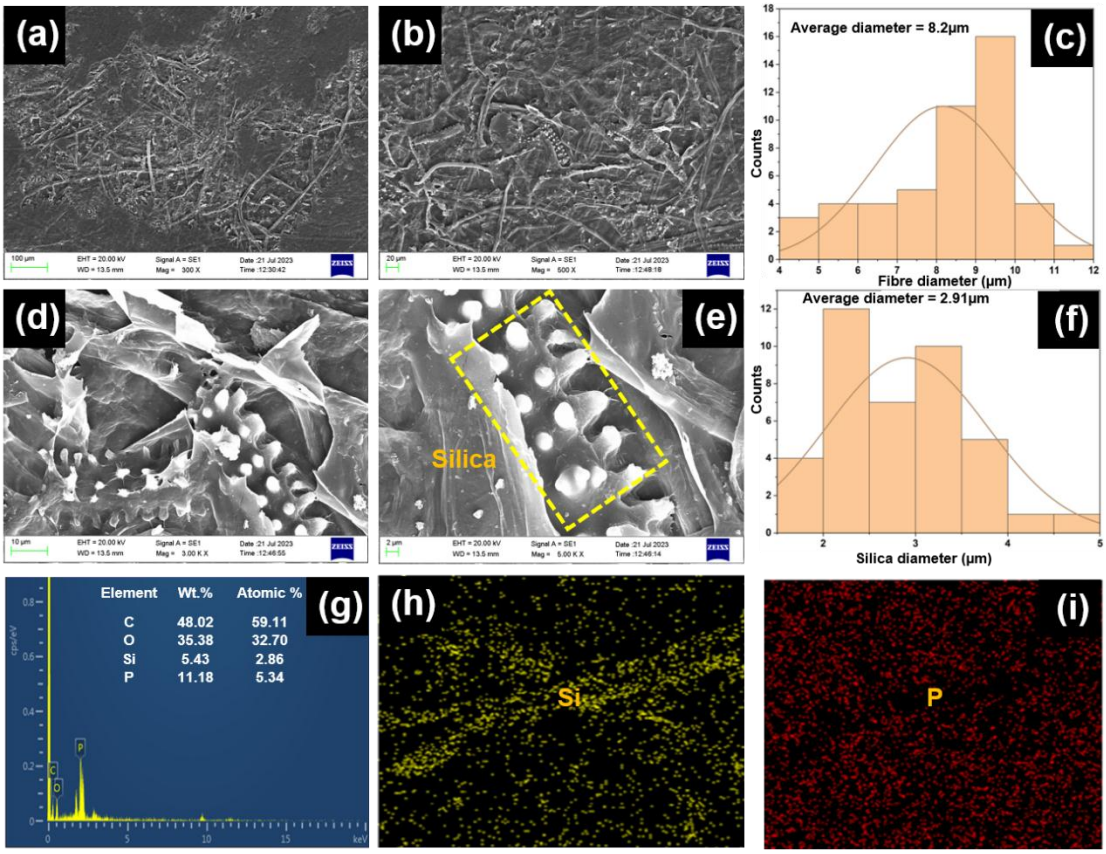

Figure 6.6 *SEM micrograph of RSF-60 at magnification (a) 300x, (b) 500x, (c) size distribution of fibers, (d) distribution of silica in RSF-60 at 2Kx, (e) 5Kx, (f) silica size distribution (g) EDX spectra of RSF-60 with their elemental composition, elemental mapping of (h) phosphorous and (i) silica.*

6.2.6 Mechanical properties of RSF

The curing time during the phosphorylation step significantly affects the mechanical properties and hydrostability of RSF films. Therefore, strength was evaluated under dry and wet conditions (***Figure 6.7*****(a-c))**. The tensile strength of dry RSF-45 and RSF-60 almost remained similar ~44.5 MPa and 47.44 MPa; however, tensile modulus improved from 293.5 MPa for RSF-45 to 387.8 MPa for RSF-60, respectively. The tensile strength and modulus of dry RSF-90 film dropped to 10.87 MPa and ~ 89 MPa, respectively, and in the case of RSF-75 film, reduced to 21.3 MPa and 210 MPa, respectively. As confirmed by XRD analysis, the introduction of

phosphate groups into the cellulose structure predominantly takes place in the amorphous regions. Consequently, this leads to a decrease in intermolecular and intramolecular hydrogen bonding interactions, resulting in a noticeable reduction in the material's crystalline structure and a substantial decline in its mechanical properties [16]. The film's tensile strength under wet conditions shows a slight reduction compared to dry conditions, with 28.6, 20.0, 13.4, and 9.51 MPa for RSF-60, RSF-45, RSF-75, and RSF-90, respectively. The corresponding tensile modulus was also found to be 3.0, 1.7, 1.2, and 0.94 MPa for the abovementioned films. The enhanced wet mechanical strength observed in RSF films can be primarily attributed to phosphate-based cross-linking with silica and improved hydrogen bonding formation, as confirmed by XPS, FTIR, and EDS analysis discussed earlier.

Bio-based cellulosic films generally aren't inherently heat-sealable and require additional adhesives to seal and package food items. Interestingly, the developed RSF films were found to be innately heat sealable without any adhesives due to the formation of silicon phosphate groups, which undergo cross-linking on local heating, making it easier for packaging applications. The film's mechanical strength was evaluated following the sealing at the middle and end portion. The tensile strength and modulus of the film sealed at the end portion were 17.4 MPa and 5.8 MPa. In contrast, the tensile strength and modulus of the film sealed in the middle were found to be 31.2MPa and 9.48 MPa, respectively **(*Figure 6.7*(c)),** and a similar observation was also observed in our previous study [614]. The findings indicate that RSF films exhibited captivatingly high strength under both dry and wet conditions, with sealibility properties forming packaging of high strength, making them a sustainable, biodegradable alternative to petroleum-derived plastics.

6.2.7 Wettability, water absorption, and swelling behavior of RSF

The contact angle of the films were investigated to determine wettability by spreading the water droplets onto its surface, as shown in ***Figure 6.7*****(d)**. The contact angle of RSF-45, RSF-60, RSF-75, and RSF-90 films were found to be 71.0°, 66.6°, 61.7°, and 54.8° respectively. The reduction in contact angle of films with an increase in surface phosphate charge could be attributed to the improved hydrogen bonding with phosphate moieties, which increases surface hydrophilicity. To understand the interaction of films with water, water absorption capacity and swelling percentage were evaluated as discussed.

The water absorption capacity and swelling percentage for all the produced films were 352.3 - 197.3 % and 91.6 – 57.3 % (as shown in ***Figure 6.7*****(e)**) due to the hydrophilic nature of cellulose phosphate. The RSF-45, RSF-60, RSF-75 and RSF-90 films had water absorption capacity of~353.3 %, 331.6 %, 197.3 %, and 237.3 % respectively. The decrease in water absorption capacity of films on increasing curing time is due to the formation of cross-link between the phosphate groups in cellulose backbone with silica present in rice straws, as confirmed through XPS studies. These cross-links limit the accessibility and mobility of cellulose chains, which makes it harder for water molecules to seep through, thus preventing swelling. Similar observations with swelling for RSF-45, RSF-60, RSF-75, and RSF-90 films were found to be 91.6 %, 67.6 %, 30.9 %, and 57.3 % respectively. The material's porous structure change during curing is responsible for decreased swelling percentage and water absorption capacity. The material's porous structure plays a key role in facilitating the entry and diffusion of water molecules. Therefore, the mechanical strength of the films was evaluated under both dry and wet conditions. Longer curing times cause material

to shrink, which reduces the size and connectivity of pores and lowers the ability of a material to absorb water. Further, RSF gels were processed into beverage cups for handling hot liquids, and the structural stability was evaluated at various temperatures and time intervals, as discussed in a subsequent section.

6.2.8 Flammability test of RSF

Inflammability tests were conducted to evaluate the ability of the films to resist direct flame or combustion, as shown in ***Figure 6.8***. The films were directly exposed to a spirit burner for 8 seconds to evaluate the burning rate and char generated. The burning rate of all the films was almost the same (0.875 cm/sec). However, the char or residual weight formed after the direct combustions were 25.8 %, 30.5 %, 36.2 %, and 45.1 % for RSF-45, RSF-60, RSF-75 and RSF-90, respectively **(*Figure 6.7*(f))**. The maximum char formation occurred in RSF-90 films due to the higher charge density of phosphate groups grafted during phosphorylation. After the flammability test, the colour of the films turned black with a glossy surface. However, the shapes and dimensions of the films remained entirely intact even after the char formation.

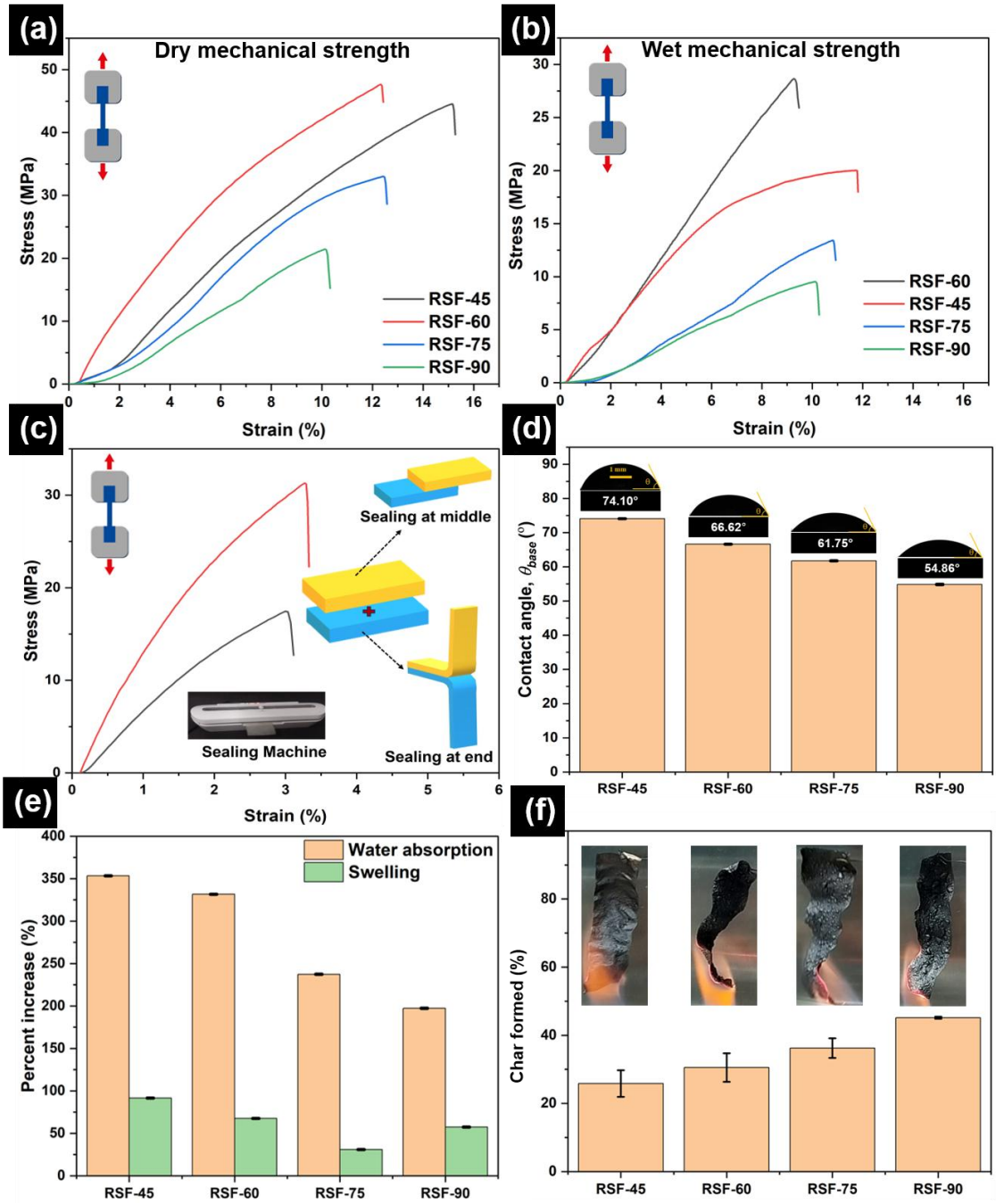

Figure 6.7 *Tensile strength of the (a) dry films, (b) wet films, (c) mechanical property after sealing, (d) contact angle, (e) water absorption and swelling property and (f) char residue formed after flammability test.*

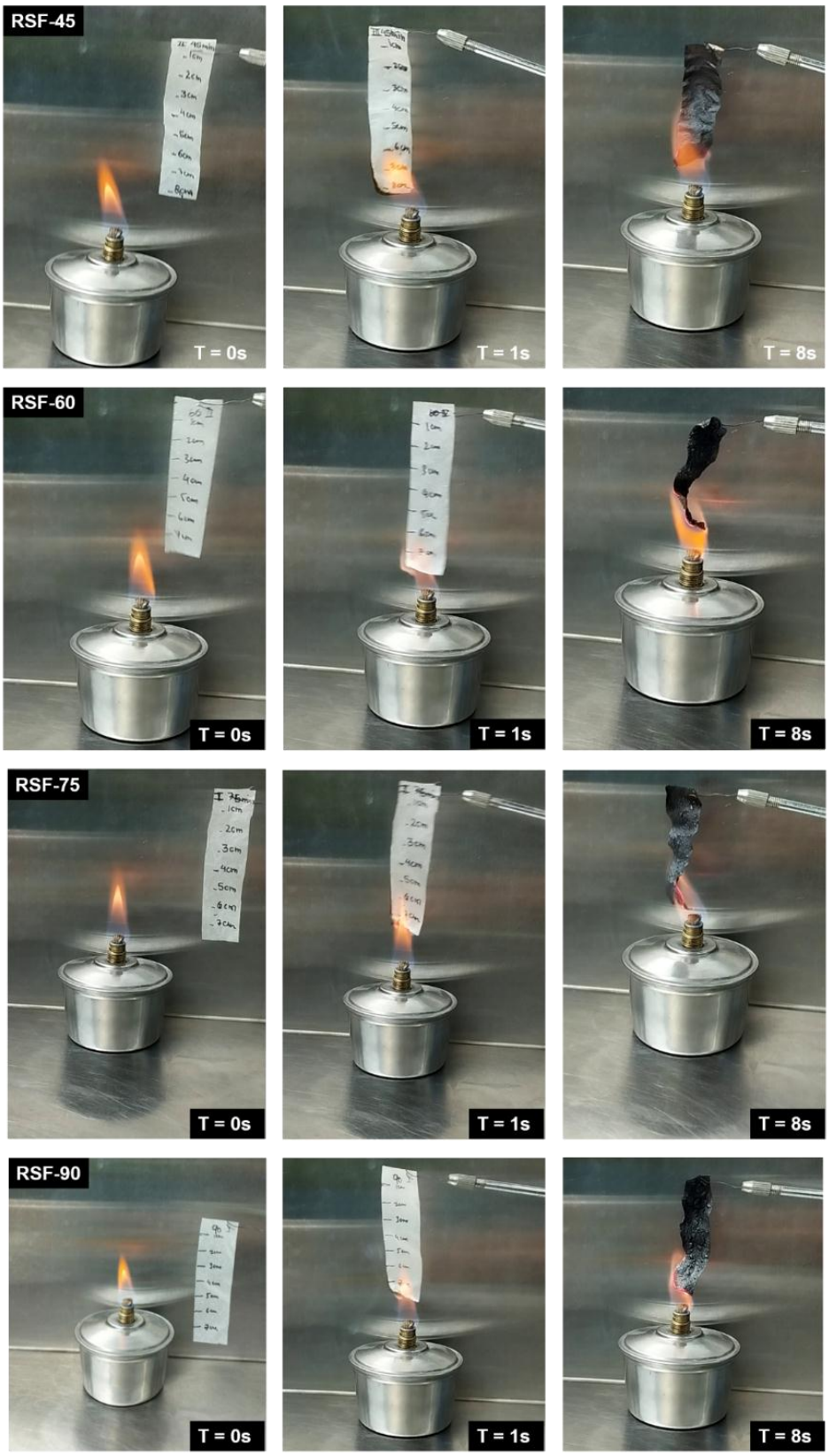

Figure 6.8 *Flammability test of the film at different time intervals (0, 1, and 8 seconds).*

6.2.9 Migration studies of RSF

The migration study was performed with two organic simulants: ethanol (as a polar solvent 10 %) and isooctane (a non-polar solvent). From ***Figure 6.10*****(a),** it was found that migration values of films were within the permissible limit in the case of both simulants' isooctane and ethanol. The maximum level of migration of film components into ethanol were 45217 ± 0.004 µg/kg, 40579 ± 0.006 µg/kg, 36714 ± 0.001µg/kg, and 37294 ± 0.008 µg/kg for RSF-45, RSF-60, RSF-75, and RSF-90 respectively. When isooctane was used as a simulant, the maximum level of migration were 22616 ± 0.006 µg/kg, 23628 ± 0.01 µg/kg, 24315.02 ± 0.001 µg/kg, and 32607 ± 0.002 µg/kg respectively. The above results conclude that the migration of films into both the simulants were within the permissible limits (60000 µg/kg) according to the current legislation (Commission Directive, 2002/72/EC). It was observed that migration increased as the CC of films increased, which could be attributed to the degradation of the cellulose backbone during curing, as well as increased swelling and solubility of RSF films. Moreover, the migrated components are cellulose derivatives, which are non-toxic, biodegradable and expected to have no immunogenic effects on human consumption. The migration of RSF films within standard limits when in contact with food simulants makes it suitable for food packaging, storage and beverage handling applications, as evaluated in the next section.

6.2.10 Application of RSF for food packaging and development of beverage cups

The developed rice film (RSF-60) was used for the packaging of easily perishable food items such as baby corn **(*Figure 6.9*(a))**, maize **(*Figure 6.9*(b))**, and apple, kiwi and pear were used for evaluation of their shelf-life properties**.**

The change in physical appearance colouration of apple, pear, and kiwi due to oxidation and weight change were studied for 7 hours at 30 °C as shown in ***Figure 6.10*****(g),** ***Figure 6.10*****(h)** and ***Figure 6.10*****(i).** The colour of the apple and pear slices turned from white to brownish, and the green texture of the kiwi went faint when placed in the open without packaging. When kept outside, apple and pear slices browning occurs due to the oxidation of polyphenol oxidase, which reacts with oxygen in the air, forming melanin. However, no significant colour changes were observed in the packaged apple, pear and kiwi slices even by the end of 7 hours. Further, the evaluation of weight change for unpacked apple slices displayed a significant loss of 92 % at room temperature in an open environment. However, the apple slice packaged with RSF-60 exhibited a lower weight loss of 42 % with no browning (***Figure 6.10*****(b)**). This suggests that the developed RSF films show a high barrier to transporting oxygen and water vapour required for food packaging applications to improve the shelf-life of stored food items. The phosphorylated gels were also utilized to develop biodegradable rice straw-based cups using an industrially-scalable molding technique and evaluated for storage of hot and cold beverages. Plastic or plastic-coated paper cups release microplastics when in contact with hot beverages, which have toxic and hazardous effects on humans and food chains [615]. Therefore, the stability of developed rice straw-based cups was evaluated at different temperature ranges (60 -100 °C) and compared with commercially available paper/plastic cups. As shown in ***Figure 6.12,*** both RSF and plastic-coated paper cups were thermally stable up to 80 °C; however, increasing temperature to 100 °C results in leaking and distortion in shape. Conversely, RSF cups showed solvothermal stability for upto 10 hours when placed at 100 °C, suggesting enhanced cellulose phosphate and silica performance for fabricating sustainable packaging materials.

The thermoregulatory capacity of the developed APTES-modified rice straw cup was evaluated with hot coffee for 90 minutes, and its comparative studies were performed and compared with the commercial plastic and paper-based cups. During the analysis, an infrared camera was used to capture the picture, record the temperature change over time, and investigate the cooling rate for the abovementioned cases. As shown in ***Figure 6.10*****(c)**, it was observed that the commercial paper cup performed better for the first 20 minutes at a 1.35 °C/min rate of cooling than the commercial plastic cup and rice straw APTES modified cup. However, after the analysis, it was observed that the rice straw APTES-modified cup performed better than the commercial paper and plastic cups. The cooling rates were 0.48, 0.59 and 0.58 °C/min, respectively. From the infrared camera image, as depicted in ***Figure 6.10*****(j),** it can be concluded that the zone of heating (red colour) over time reduced, which confirmed the phenomenon of the cooling process. The temperature difference between the outer boundary of the cups and fluid (coffee) placed inside was highest for the rice straw APTES-modified cups (as shown in ***Figure 6.10*****(d)**), and it was around 18.3 °C, 8.1 °C, 3.4 °C and 2.4 °C at 0, 30, 60 and 90 minutes. However, the temperature difference for commercial paper cups was around 14.2 °C, 5.5 °C, 4.3 °C, and 3 °C; plastic cups were around 12.8 °C, 3.7 °C, 3.2 °C and 1.9 °C at 0, 30, 60 and 90 minutes. These results suggest that the rice straw APTES-modified cups performed better and somehow showed the packed fluids' thermal stability due to inherent silica and APTES modification.

To check the wettability of developed RSF cups, hot coffee was poured **(*Figure 6.10*****(e)),** and absorption capacity was evaluated at different time intervals. It was observed that after 420 minutes, approximately 20 mL of coffee was absorbed in RSF cups, forming a brown coffee strain at its boundaries (both at the inner and outer layers).

RSF cups were modified using 3-(aminopropyl)triethoxysilane (APTES) to overcome this limitation and improve wettability. Interestingly, modified RSF cups show no absorption of coffee with the absence of stains at inner and exterior walls throughout 420 minutes. Furthermore, the effervescence properties **(*Figure 6.10*(f)** of the cold drinks were evaluated using disposable plastic cups and RSF cups. During the analysis, it was observed that a large volume of supersaturated carbon dioxide evolved from the surface of the plastic glass upon pouring the cold drink. However, in the RSF glass, fizzing was observed only a few seconds later; no fizzing was observed during the whole analysis period. Additionally, the washability of the developed cups after use (after drinking coffee) was tested using 0.5 % chlorite solution, which resulted in the complete removal of coffee stains with improved reusability of cups up to three times (as shown in ***Figure 6.11***). In this study, RSF cups developed through strategic functionalization approaches show high thermal stability, reduced wettability and easy holding experience required for consuming hot and cold beverages. This makes them sustainable, economical and healthy, non-toxic alternatives to plastic-coated paper or cups.

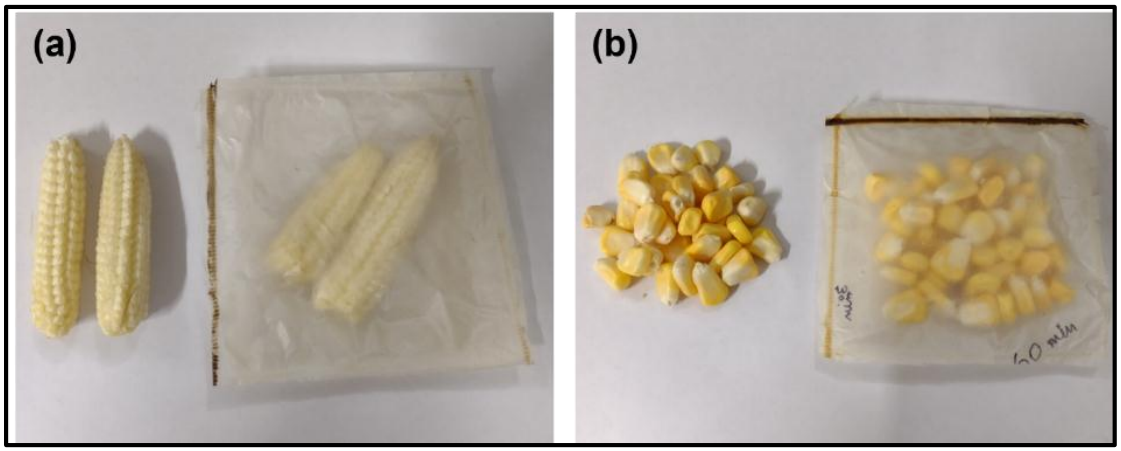

Figure 6.9 *Photograph of packed (a) baby corn and (b) maize using rice straw film.*

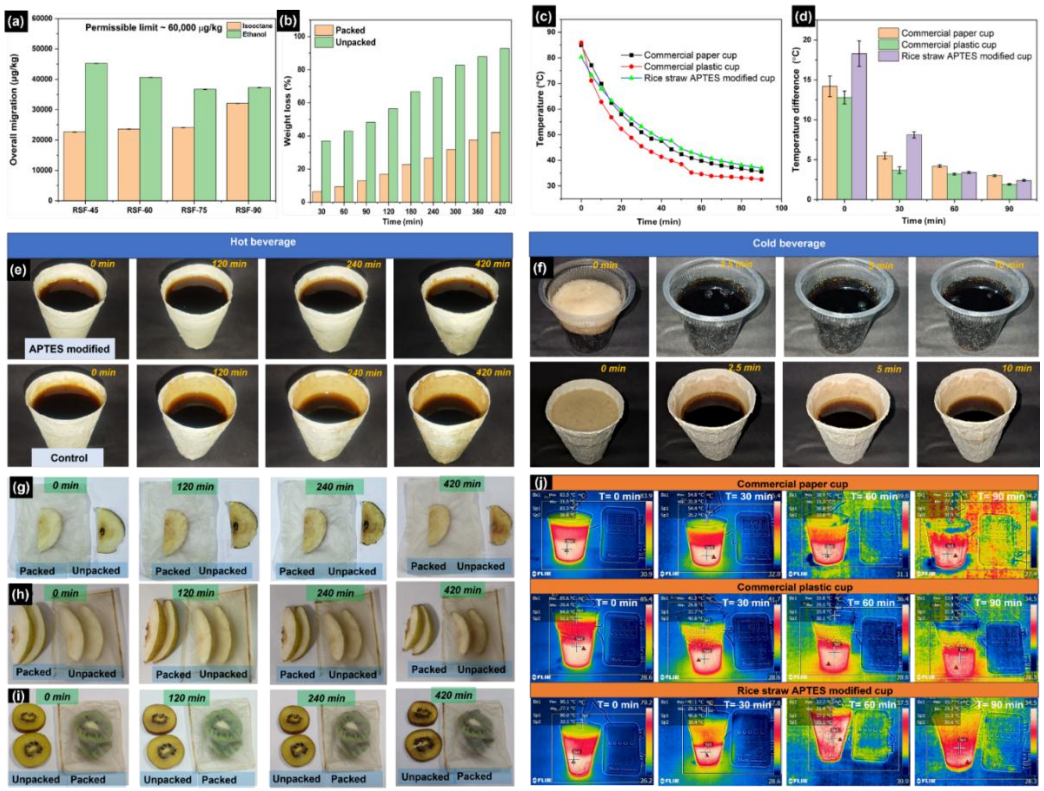

Figure 6.10 *(a) Overall migration of RSF films in ethanol and isooctane, (b) loss in weight of apple in packed and unpacked conditions, (c) thermoregulatory studies of coffee with commercial paper cup, plastic cup and rice straw APTES modified cups measured in term of cooling rate, (d) temperature difference between boundary wall and coffee filled cups with time, (e) photograph of coffee filled RSF and APTES modified cups to demonstrate staining at different intervals of time, (f) photographs of the cups (plastic disposable and rice straw cup) filled with cold drinks to study the effects of anti-fizzing properties, photographs of (g) apples (h) pear and (i) kiwi taken at different interval of time in packed and unpacked condition, and (j) thermal images of coffee filled in commercial paper cup, plastic cup and rice straw cup at different time intervals.*

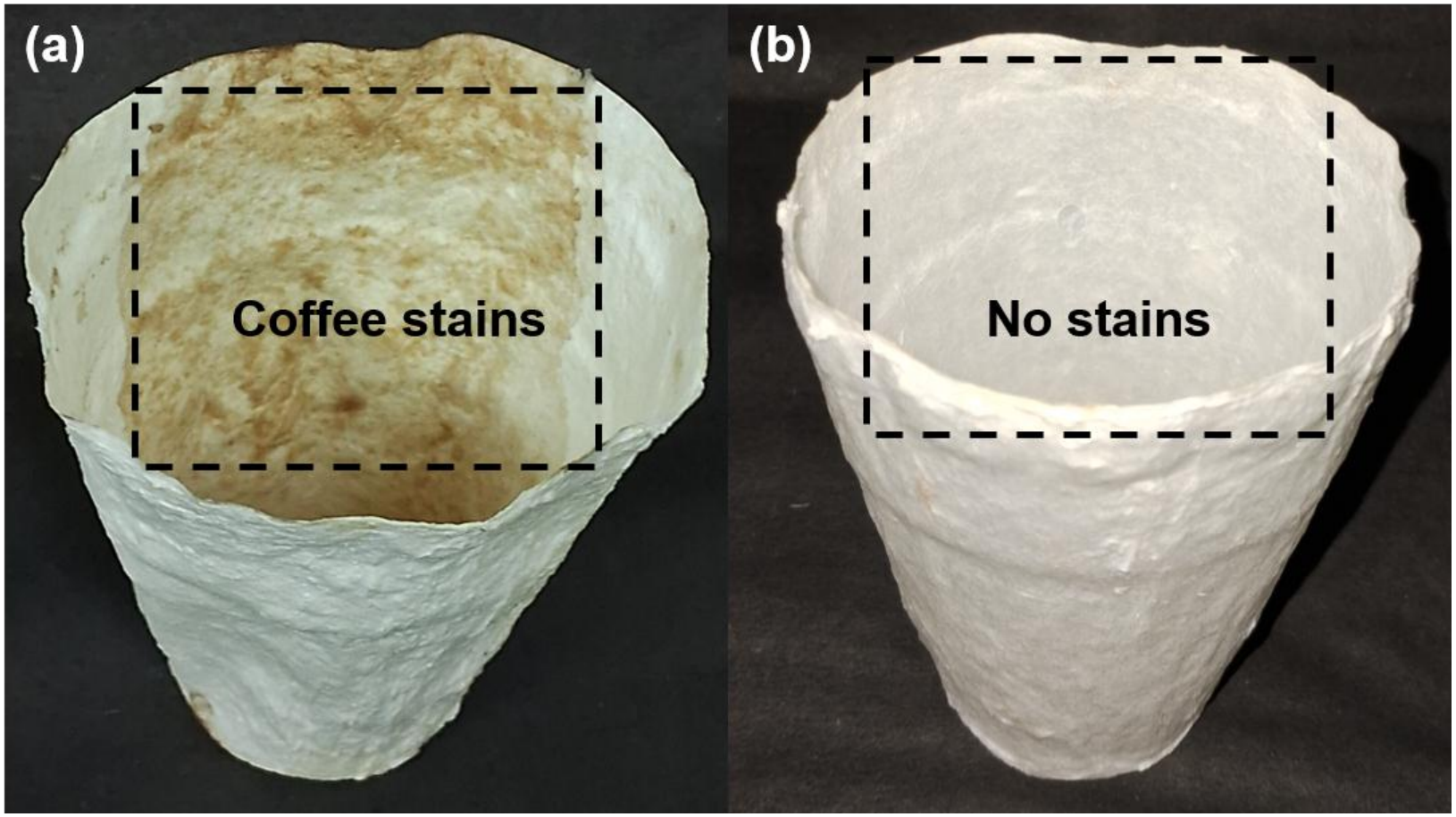

Figure 6.11 *Photograph of the rice cups after its utilization for drinking coffee (a) and the removal of stains after washing(b).*

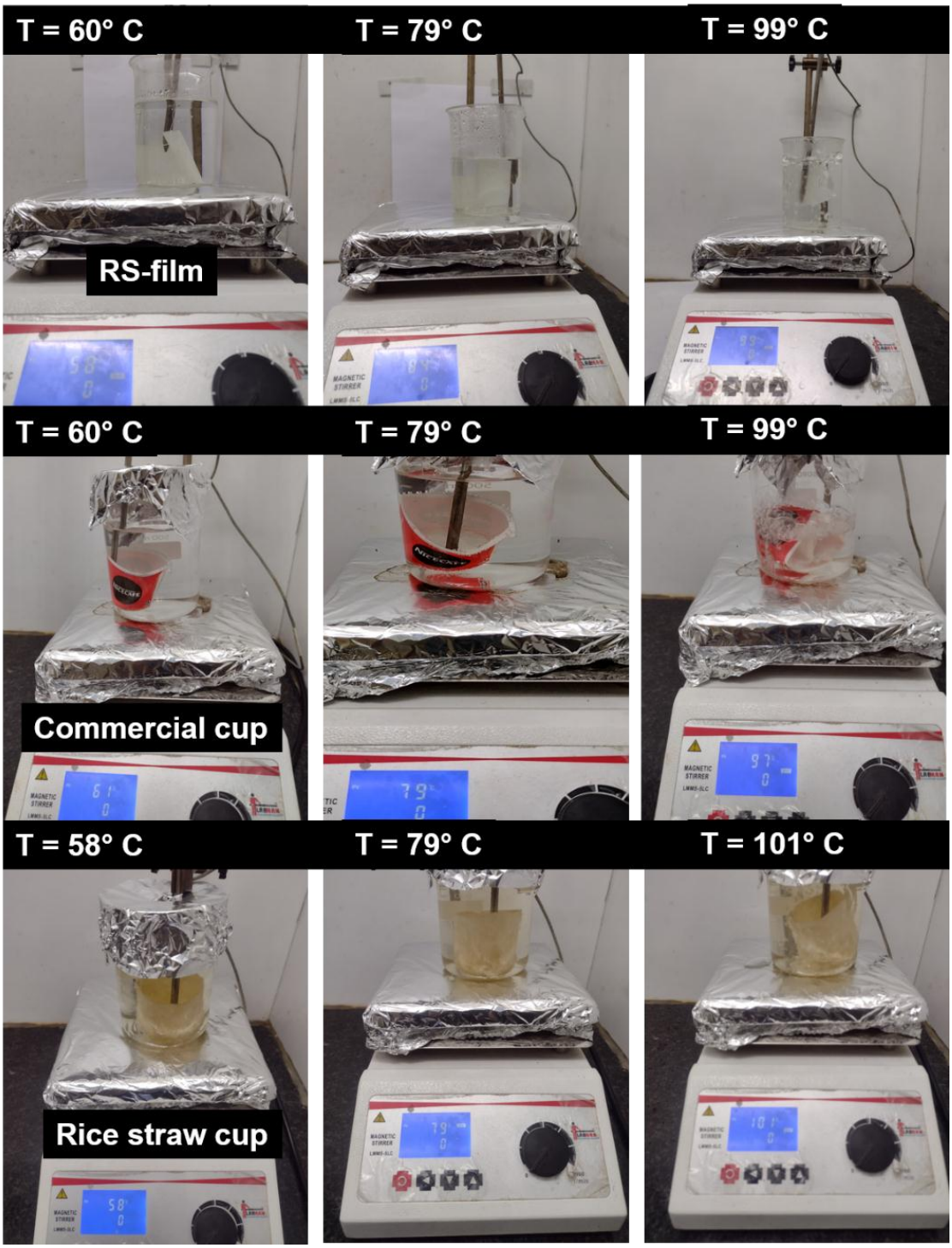

Figure 6.12 *Presents the test for (a) hot water stability of the developed phosphorylated rice straw film, (b) hot water stability of the commercial cup, and (c) hot water stability of the developed phosphorylated rice straw cups.*

6.3 Production of RS aerogel and thermal box

In this work, aerogel with lightweight, low density (0.028-0.049 g/cm^3), high porosity (97% - 98 %), charge content (1250 mmol/kg), and low thermal conductivity (0.053-0.067 W/mK) properties were produced from rice straw *via* the delignification phosphorylation, homogenisation, freezing and lyophilisation method. The compressive strength of the aerogel (RSA-60) was in the range of 0.052-0.273 MPa at different strains percent (20% - 80%). The water absorption capacity of the developed aerogel was found to be in the range of 1420- 2411 %, which improved with increased curing time. The developed aerogels were highly porous with distributed silica and were observed in the SEM image. The grafting of phosphate ions on the surface of DRS and the presence of silica were confirmed by FTIR, EDS, and XPS. The developed boxes were utilised to store butter and maintain their original structure without melting. The developed aerogels were also utilised for packaging butter and found to improve the shelf life of butter to 7 days without the growth of pathogenic bacteria.

6.3.1 Density, porosity, thermal conductivity, and water absorption properties of RSA

The apparent density of the produced aerogels increases by increasing the curing time of the aerogels (RSA-45 (0.028 g/cm^3), RSA-60 (0.037 g/cm^3), RSA-75 (0.04 g/cm^3), and RSA-90 (0.049 g/cm^3)). During the freeze drying, all the water molecules present sublimate, and only solid content of porous matrix remains; therefore, the overall density of the produced aerogels decreases. However, there were slight differences in the porosity of the produced aerogels, ranging between 96-98 % **(*Figure 6.13*(b))** shows the effect of curing time and the CC on the water absorption capacity of the developed aerogels (RSA-45, RSA-60, RSA-75, and RSA-90). As the curing

time of phosphorylation increases, phosphate content in the produced aerogel decreases, and the maximum CC was obtained in the RSA-45 (1250 mmol/kg) followed by RSA-60, RSA-75, and RSA-90, as shown in ***Figure 6.14*****(a-d)** The decrease in phosphate content resulted in lower water absorption capacity. The water absorption capacity of RSA-45 was the highest (2411.5 %) among all the produced aerogels, RSA-60 (1660.8 %), RSA-75 (1578.6), and RSA-90 (1420.6 %). The absorption capacity of the aerogels increased with an increase in porosity and phosphate groups. Phosphate being negatively charged creates electrostatic repulsion between adjacent cellulose chains. This repulsion causes the cellulose chain to spread out and cause conformational change, which improves the accessible surface area to accommodate a large number of water molecules, hence improving water absorption. Incorporating phosphate groups offer the cellulose molecule a polar nature, which improves the interactions between water molecules and phosphorylated cellulose. This enhanced interaction resulted in a stronger affinity for water, thus increasing the water absorption capacity. Since the porous structure of the aerogels contains more than 90% of air, it provides good thermal insulation properties. The developed aerogels' thermal conductivity (***Figure 6.13*****(c))** ranges between 0.053-0.067 W/mK. The RSA-45 had minimum thermal conductivity ranging from 0.054-0.053 W/mK, 0.064-0.062 W/mK for RSA-60, 0.063-0.061 W/mK for RSA-75 and maximum 0.067-0.065 W/mK for RSA-90. The thermal conductivity for these aerogels decreases with an increase in the temperature and a decrease in the porosity. The RSA-45 had a maximum of 98% porosity, which was reduced to 96% for the RSA-90. As the porosity of the aerogels increases, the maximum volume/space occupied by the air molecules decreases the thermal conductivity of the materials, as air is known as a good thermal insulator [577].

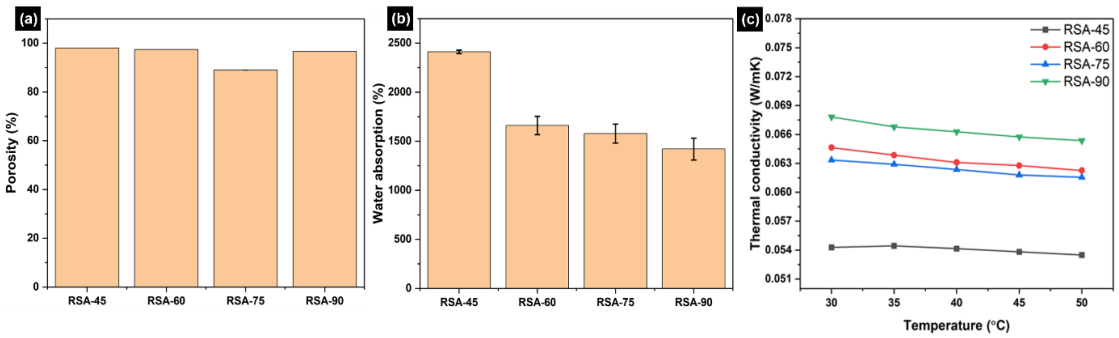

Figure 6.13 *Presents (a) porosity, (b) water absorption and (c) thermal conductivity of phosphorylated RS aerogels.*

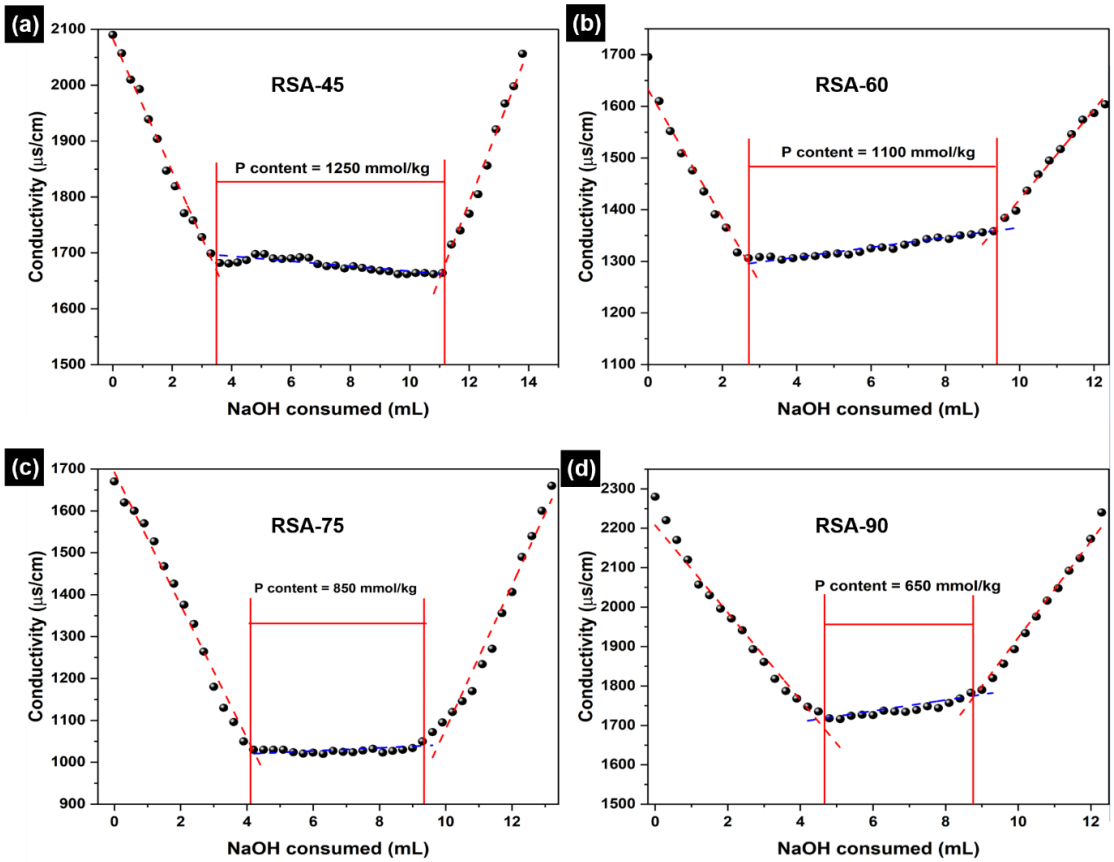

Figure 6.14 *Charge content of (a) RSA-45 (b) RSA-60 (c) RSA-75 (d) RSA-90 in the produced aerogels after different curing times.*

6.3.2 Mechanical property of RSA

The mechanical property of the aerogel defines its applicability for different applications; therefore, the compressive strength of the developed aerogel was studied to assess its structural integrity, durability, and strength. According to the data presented

in ***Figure 6.15***, there was a positive correlation between the strain percentage and the compressive strength of RSA-45, indicating that the compressive strength increased with a gradual increase in strain percentage. The maximum compressive strength of RSA-45 aerogel was ~ 0.052 MPa at 20 % strain, which further increased to 0.118 MPa at 40 % strain, 0.163 MPa at 60 %, and 0.273 MPa at 80% strain, as presented in ***Figure 6.15*****(a)**. The increase in the compressive strength on a gradual increase in shear strain was due to the densification of aerogel on applied shear stress. At 20, 40, 60, and 80 % strain compressive modulus were 0.26, 0.295, 0.27, and 0.34 MPa, respectively. A cyclic compression test for RSA-45 was also performed for five different cycles for 30, 60, and 80 % strain, resulting in a significant decrease in the maximum stress for the first three cycles, then almost remained unchanged for 4th and 5th cycles, as shown in ***Figure 6.15*****(b)**. The findings revealed that the RSA-45 aerogels exhibit remarkable durability and resistance to fatigue under repeated compression, making them highly suitable for long-term use.

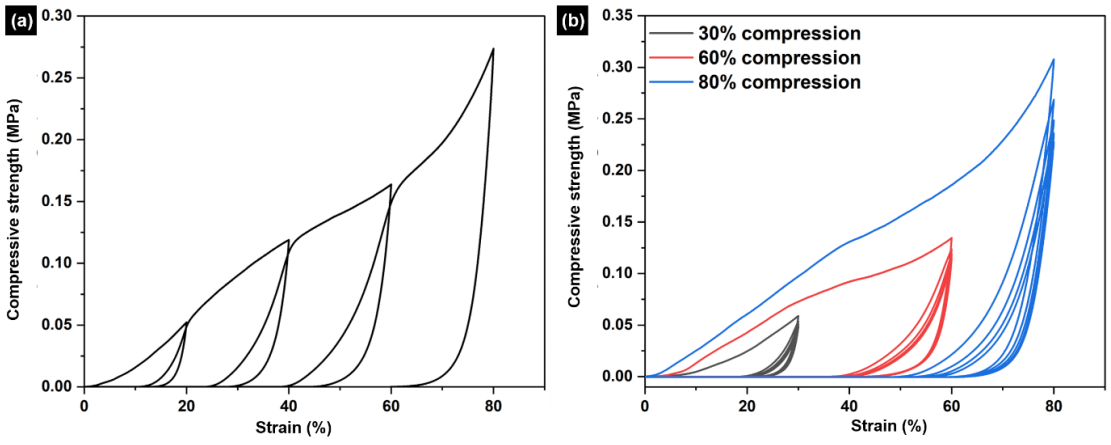

Figure 6.15 *Compressive properties of RSA-45 under (a) different strain percentage in a single cycle and (b) multiple cycle compression under different applied strain%.*

6.3.3 LCA of RS aerogel and its comparison with polyurethane foam production

Life Cycle Assessment (LCA) was conducted to evaluate the environmental impacts associated with the development of boxes made from phosphorylated rice aerogel, and these impacts were compared to those of commercially accessible polyurethane foam (***Figure 6.17*(a-c)**). The climate change category exhibited the most significant environmental impact, with values of 21.8 kg CO_2 eq. in both excluding and including biogenic carbon, 2.11 kg 1,4-DB eq., and 4.78 kg oil eq., in terrestrial ecotoxicity and fossil depletion categories, respectively. The primary sources of environmental impact in rice aerogel production stem from electricity-intensive processes like delignification, phosphorylation, and freeze-drying. The production process of polyurethane foam boxes resulted in significant environmental impacts across three categories: climate change (excluding and including biogenic carbon), terrestrial ecotoxicity, and fossil depletion. The respective values for these impacts were 25 kg CO_2 eq., 21.8 kg 1,4-DB eq., and 6.23 kg oil eq. The production of aerogel resulted in minimal environmental impact values in three distinct categories: marine eutrophication (6.49×10^{-5}, kg N eq.), stratospheric ozone depletion (3.37×10^{-6} kg CFC-11 eq.), and freshwater eutrophication (1.38×10^{-6} kg P eq.). On the other hand, polyurethane foam had almost negligible adverse environmental effects in terms of marine eutrophication (2.87×10^{-5} kg N eq.), stratospheric ozone depletion (4.91×10^{-6} kg CFC-11 eq.), and freshwater eutrophication (2.43×10^{-6} kg P eq.). The primary sources of environmental impact in the production of PU foam boxes stem from the energy-intensive processes involved in polyol production and extrusion moulding.

6.3.3.1 Normalization of midpoint results RS aerogel polyurethane foam production

The midpoint result was normalised to screen the dominant ecological impact categories influencing rice aerogel and polyurethane boxes' production (***Figure 6.17*(a)** and ***Figure 6.17*(b)).** Among the 18 environmental impact categories, fossil depletion (0.0048 kg oil eq.), climate change (excluding biogenic carbon, 0.0027 kg CO_2 eq.), and photochemical ozone formation (0.0019 kg NO_x eq.) in ecosystems were observed to have the highest values after normalisation of midpoint results which indicates that upon production of rice aerogel box, it will put a deteriorating impact on fossil resources and atmospheric ecosystem. Conversely, when it comes to polyurethane aerogel box production, the dominant categories were fossil depletion (0.0063 kg oil eq.), photochemical ozone formation (0.0056 kg NO_x eq.), and terrestrial acidification (0.0039 kg SO_2 eq.). This suggests polyurethane foam box production harms fossil resources and the atmospheric and soil ecosystems. For rice aerogel and polyurethane box production, the ecological impact in fossil depletion, terrestrial acidification, photochemical ozone formation and climate change comes from the consumption of electricity as an energy source derived from fossil hard coal.

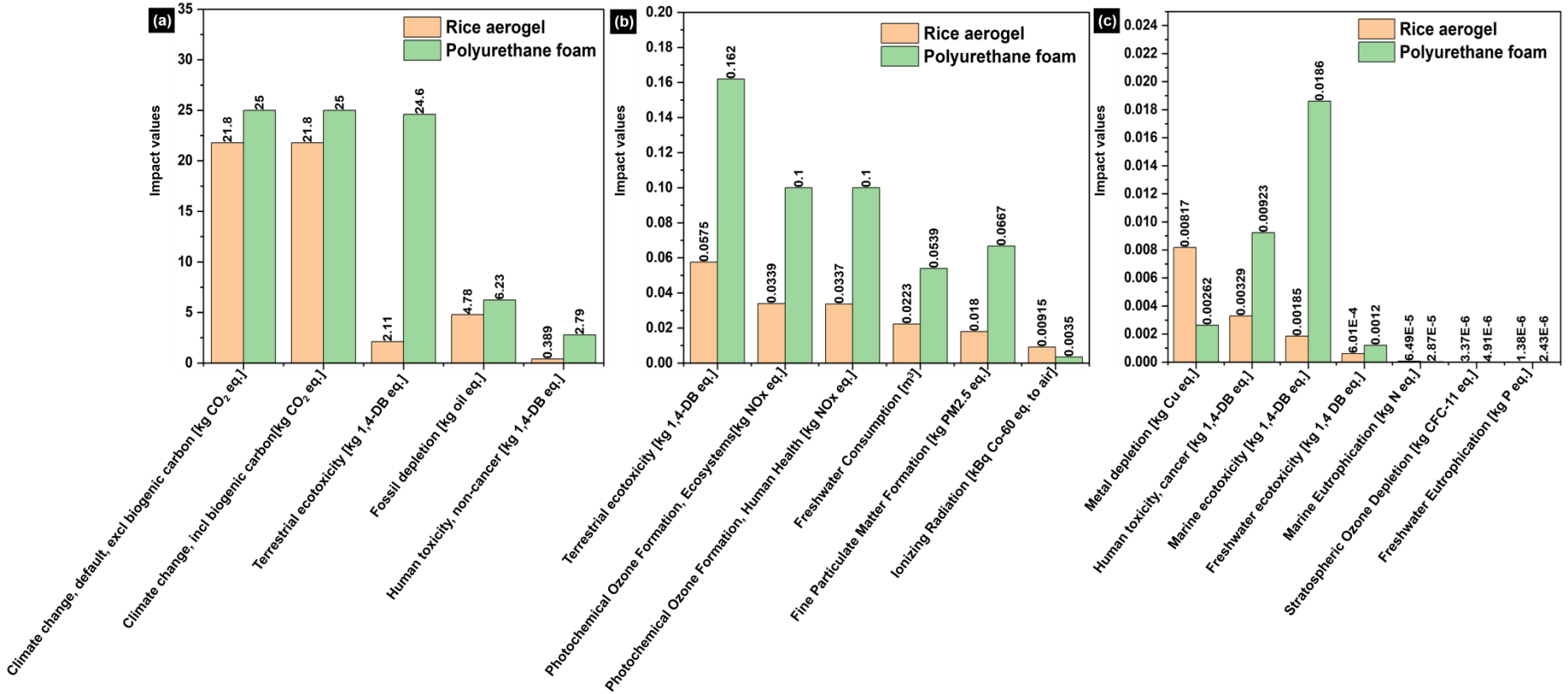

Figure 6.16 *LCA based comparison of the environmental impacts generated in different categories during rice aerogel and PU foam production.*

A possible strategy to reduce the ecological impact of aerogel production would be replacing the electrical energy from fossil resources with alternate, sustainable energy sources. Moreover, using energy-efficient instrumentation during the scalable production of rice aerogel boxes can also reduce the environmental impact generated. Based on these midpoint normalised results, we have identified fossil depletion, photochemical ozone formation, terrestrial acidification, and climate change (excluding biogenic carbon) as the dominant environmental impact categories, which will be the focus of our sensitivity analysis.

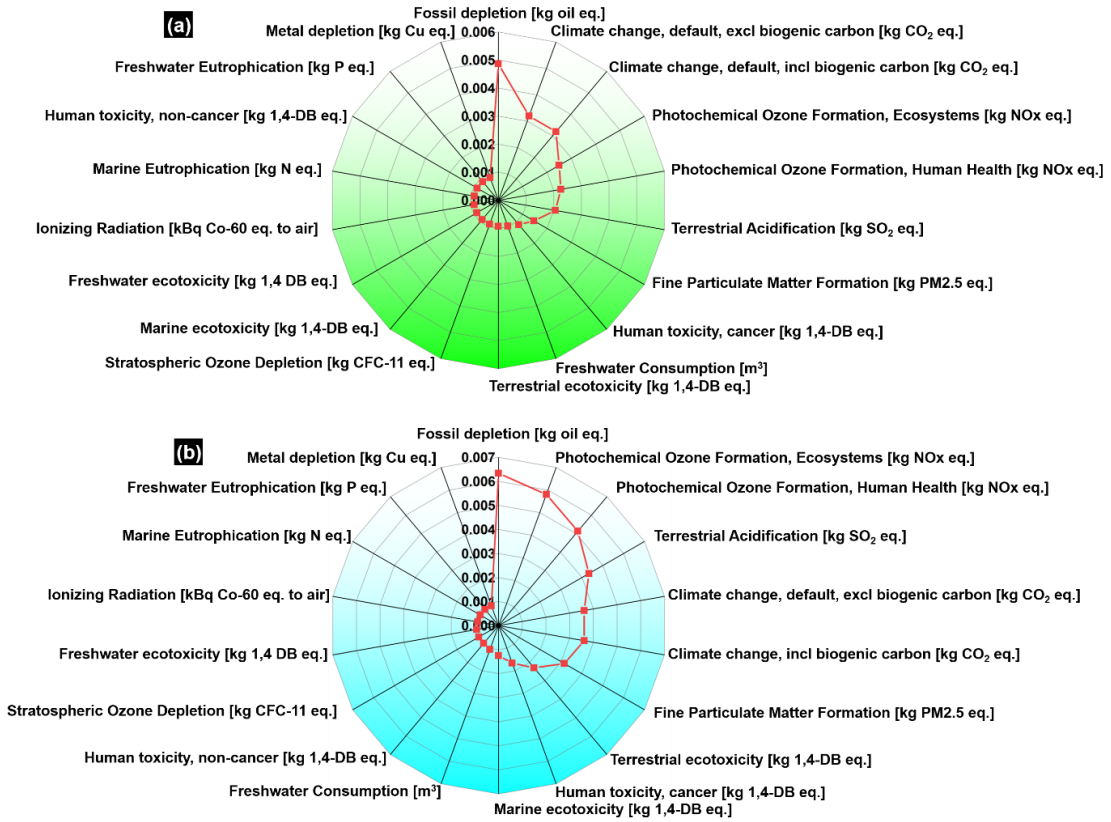

Figure 6.17 *Radar graph of normalised midpoint results for rice aerogel box and polyurethane box production.*

6.3.3.2 Sensitivity analysis RS aerogel and polyurethane foam production

The sensitivity analysis was carried out to observe the effect of processes used during the production of rice aerogel boxes on the environmental impact. During the midpoint results, it was observed that electricity contributes majorly to the environmental impact. From the normalisation results (***Table 6.3***), climate change, fossil depletion and photochemical ozone formation were observed to be the dominant category and changes in their impact values upon positively and negatively varying the input values for electricity consumption, delignification, and phosphorylation were studied using sensitivity analysis. For electricity, it was observed that a 10% increase resulted in a similar rise in the value of climate change fossil depletion and photochemical ozone formation. In contrast, on reducing the electricity input by 8%, a similar reduction in the values was observed. For delignification and phosphorylation, however, the increase in the input value (10%) enhances the impact values of climate change fossil depletion and photochemical ozone formation by 5.05%, 4.81%, and 4.72% for delignification and 3.21%, 3.35% and 3.24% for phosphorylation respectively. A reduction in the input values for both delignification and phosphorylation decrease the values of climate change fossil depletion and photochemical ozone formation by -3.67%, -3.97% and -4.13% for delignification and 2.75%, 2.72% and 2.65% for phosphorylation. For polyurethane foam boxes, three processes, i.e., electricity, polyol production and polyol to polyurethane production, were considered for sensitivity analysis. For changes in the input values of electricity, a 10% increase enhances the impact value of fossil depletion, photochemical ozone formation, and terrestrial acidification by 8.83%, 10%, and 9.88%. In contrast, an 8% decrease in electricity values would reduce the impact values by 6.26%, 7.0% and

7.41%. Polyol production also influences the dominant ecological impact category majorly as with a 10% increase in the input values of polyol production, a 7.7%, 90% and 8.64% increase in the impact values were observed for fossil depletion, photochemical ozone formation, and terrestrial acidification respectively whereas 8% decrease in input value reduces the impact values by 5.94%, 6.6% and 6.79%. The conversion to polyurethane is a simple process with low consumption of chemicals and energy, which suggests its low influence on the changes in the ecological impact of the dominant category, as observed from ***Table 6.4.*** The sensitivity analysis indicates that variation in inputs for electricity significantly influences the ecological impact of rice aerogel box production, followed by delignification and phosphorylation. In contrast, electricity and polyol production significantly affected the ecological impact generated by polyurethane boxes.

Table 6.3 *Sensitivity analysis of the dominant environmental categories for producing rice aerogel boxes.*

Categories	**Electricity**		**Delignification of rice straw**		**Phosphorylation**	
	10% increase	8% decrease	10% increase	8% decrease	10% increase	8% decrease
Climate change	10.09	-7.80	5.05	-3.67	3.21	-2.75
Fossil depletion	10.04	-7.95	4.81	-3.97	3.35	-2.72
Photochemical Ozone formation	9.73	-7.96	4.72	-4.13	3.24	-2.65

Table 6.4 *Sensitivity analysis of the dominant environmental categories for producing polyurethane foam-based boxes.*

Categories	**Electricity**		**Polyol**		**Polyol to polyurethane**	
	10% increase	8% decrease	10% increase	8% Decrease	10% increase	8% decrease
Fossil depletion	8.83	-6.26	7.70	-5.94	0.80	-0.48
Photochemical ozone formation,	10. 00	-7.00	9.00	-6.60	1.00	0.00
Terrestrial Acidification	9.88	-7.41	8.64	-6.79	0.00	0.00

6.3.4 Functional properties of RSA

Effects of delignification on rice straw waste and phosphorylation on the functional properties of the delignified rice straw were analysed through FTIR, as shown in ***Figure 6.18*****(a).** The peaks at 1045 cm^{-1}, 1630 cm^{-1}, 2925 cm^{-1}, and 3320 cm^{-1} were present in all the samples (DRS, RSA-45, RSA-60, RSA-75, and RSA-90) presenting the C-O vibrational bond [616], C=C bond (stretching vibration), C-H stretching vibration, and O-H vibration which are the characteristics peaks of cellulose [617–620]. After the phosphorylation of DRS at different curing times, two new and distinct peaks at 824 cm^{-1} and 915 cm^{-1} were observed, and these peaks correspond to the P-O bond and P-OH bond, respectively [509,603]. The 1160 cm^{-1} and 1436 cm^{-1} peaks in developed aerogels (RSA-45, RSA-60, RSA-75, and RSA-90) present the C-O-C asymmetric vibration of cellulose linkage and -CH_2 bending [15,518]. The peaks around 1045 cm^{-1} are present in all the samples and represent the Si-O-Si bond, possibly due to inherent silica on the surface of rice straw [621]. To conduct a more detailed examination of the phosphate modification of DRS and the presence of silica in RSA-45, XPS was utilised to analyse the chemical composition of the RSA-45 aerogel surface, as shown in ***Figure 6.18***. The survey scan of RSA-45 (***Figure 6.18*****(b)**)

revealed distinct peaks at specific binding energies: 103.03 eV for *Si2p*, 134.0 eV for *P2p*, 284.0 eV for *C1s*, and 532.08 eV for *O1s*. These peaks correspond to the respective bonds of silicon, phosphate, carbon, and oxygen. ***Figure 6.18*(c)** presents the high-resolution analysis of the *P2p* spectrum, revealing deconvoluted peaks at binding energies of 132.8 and 133.6 eV, which can be attributed to the P-O/P-C and P-O-C bonds, respectively, as supported by previous studies [622,623]. Similarly, the high-resolution broad spectrum of *Si2p* in ***Figure 6.18*(d)** demonstrates deconvoluted peaks at 101.9 and 102.7 eV, indicating the presence of Si-O-C and Si-C bonds, respectively [624,625]. The deconvoluted peaks observed in the broad *O1s* spectrum (as shown in ***Figure 6.18*(e)**) correspond to the P=O and P-O bonds, with binding energies of 531.5 and 532.3 eV, respectively [238,626]. In the broad spectrum of *C1s* displayed in ***Figure 6.18*(f)**, the deconvoluted peaks at 284, 286, and 287 eV can be attributed to the C-C/C-H, O-C-O, and C=O bonds, respectively [627,628]. The presence of P=O, P-O-C, P-O, and P-C bonds in the *O1s* and *P2p* broad spectrum, as well as Si-O-C and Si-C bonds in the *Si2p* broad spectrum, provides evidence that phosphate and silica are present in the developed aerogels (RSA-45). The possible mechanism for the phosphorylation of rice straw is presented in ***Figure 6.18*(h)**, where the presence of silica microparticles was shown on the surface of rice straws and the P-O-C bonding with the -OH groups of *C6* of cellulose.

6.3.5 Thermal properties of RSA

The thermal stability of DRS, RSA-45, RSA-60, RSA-75, and RSA-90 aerogels was investigated from the TGA curve between residual weight and temperature, as shown in ***Figure 6.18*(g)**. The initial degradation of all the samples started between the 96-100 °C temperature range, which resulted in ~ 4-5% weight loss, possibly due to water molecules' evaporation or the moisture present. The 10% degradation of the DRS

was achieved at 263.5 °C, which was higher than all the produced aerogels (RSA-45, RSA-60, RSA-75, and RSA-90). After undergoing phosphorylation, the phosphate group attached to the DRS functions as a catalyst, leading to accelerated dehydration and causing the cellulose backbones to decompose prematurely [15]. For DRS, a maximum weight loss of ~66% was observed at 356.6°C; however, in the produced aerogels, the maximum degradation of 37-38% was observed in the temperature range of 280-285 °C. The residual weight produced at 700 °C was (37-38%) for aerogels RSA-45, RSA-60, and RSA-75,31.5% for RSA-90, and ~11% for DRS. These considerable differences in the residual weight formation might be due to the grafting of phosphate groups at the *C6* position of the native cellulose structure responsible for ceasing the thermal decomposition of cellulose [15,205].

6.3.6 Structural properties RSA

The effects of phosphorylation on the structural properties of delignified rice straw and the produced aerogels are shown in ***Figure 6.19***. The peaks at 22.02° and 16.4° in the DRS are the characteristic peaks of cellulose I representing crystal lattices of (110) and (002) [629,630]. The *d*-spacing of the DRS sample at 22.02° and 16.4° were 2.05 *Å* and 2.73 *Å* and crystal sizes were 0.41 *Å* and 0.37 *Å* respectively. The crystallite size and the *d*-spacing at 20.2° in RSA-45, RSA-60, and RSA-75 aerogels were 0.11 and 2.23 Å. The peaks at 22.02° and 26.4° of DRS merged and shifted slightly toward a lower angle at 20.2° in the RSA-45, RSA-60, and RSA-75 (110). The crystallinity index of the DRS significantly reduced the due to phosphorylation reaction, homogenisation and freeze-drying processes involved in the production of aerogels. The *CI* of the DRS was 80%, which reduced to 64.6%, 66%, and 43.8% for produced aerogels RSA-45, RSA-60, and RSA-75, respectively. The change in the diffraction pattern and *CI* of DRS was mainly due to phosphorylation, homogenisation,

and lyophilisation. During the homogenisation, high shear and tear forces are generated, responsible for the disruption of hydrogen bonding and the glycosidic linkages present between the cellulose fibrils, thus damaging the crystalline region and responsible for reduced *CI* [578]. The decline *CI* observed in RSA-45, RSA-60, and RSA-75 on phosphorylation could result from cellulose fibril dissolution at different curing times.

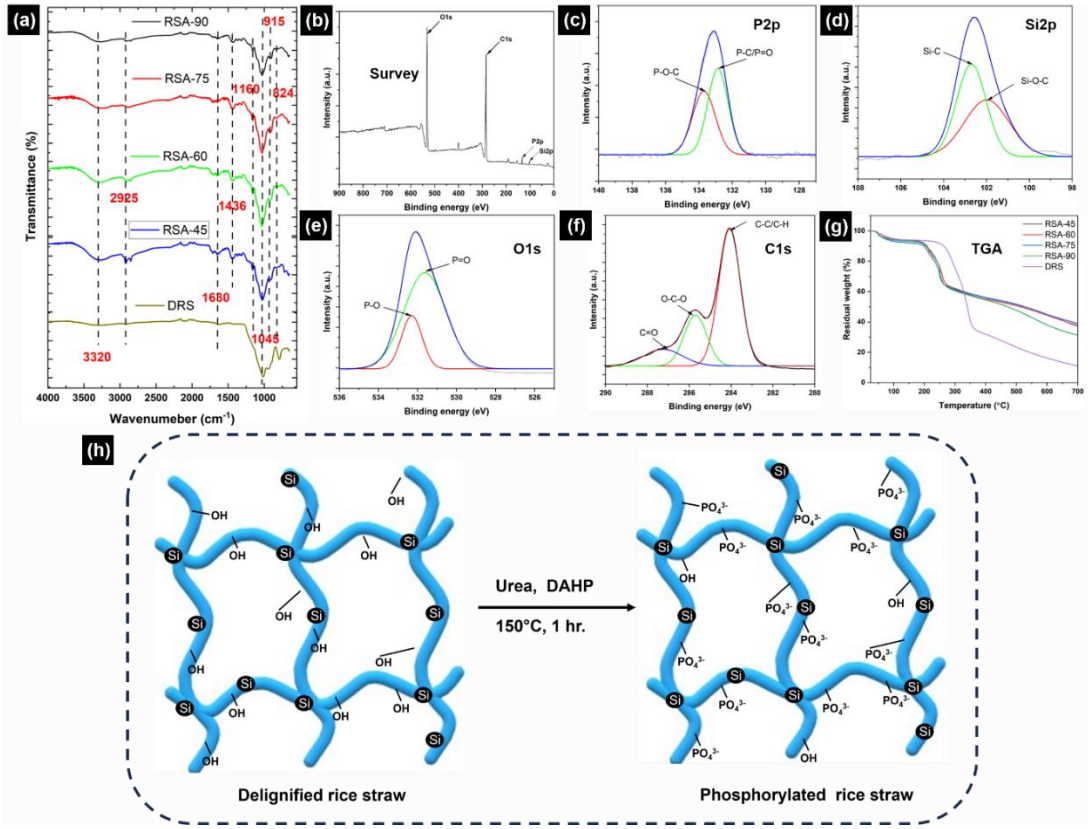

Figure 6.18 *Represent (a) FTIR spectra of aerogels and DRS, (b) XPS survey of RSA-45, (c)- (f) display the broad spectra of P2p, Si2p, O1s, and C1s, respectively, (g) thermal properties and (h) mechanism of phosphorylation reaction.*

As the cellulose fibrils dissolve, the internal structure of the cellulose fibres undergoes disruption and rearrangement, leading to a reduction in crystallinity [193]. Furthermore, a peak shift from 20.2° to 14.8° was observed in the RSA-90 aerogel sample. This shift in the prepared aerogels might be due to the prolonged curing time of 90 minutes during the phosphorylation reaction. However, the *CI* of the RSA-90 was ~ 57%. The crystallite size and *d* spacing at 14.8° were 0.12 Å and 3.01 Å, respectively.

The phosphorylation reaction decreased the peak intensities of the developed aerogels, indicating a disruption in the cellulose crystal structure, leading to a reduction in crystallinity [631].

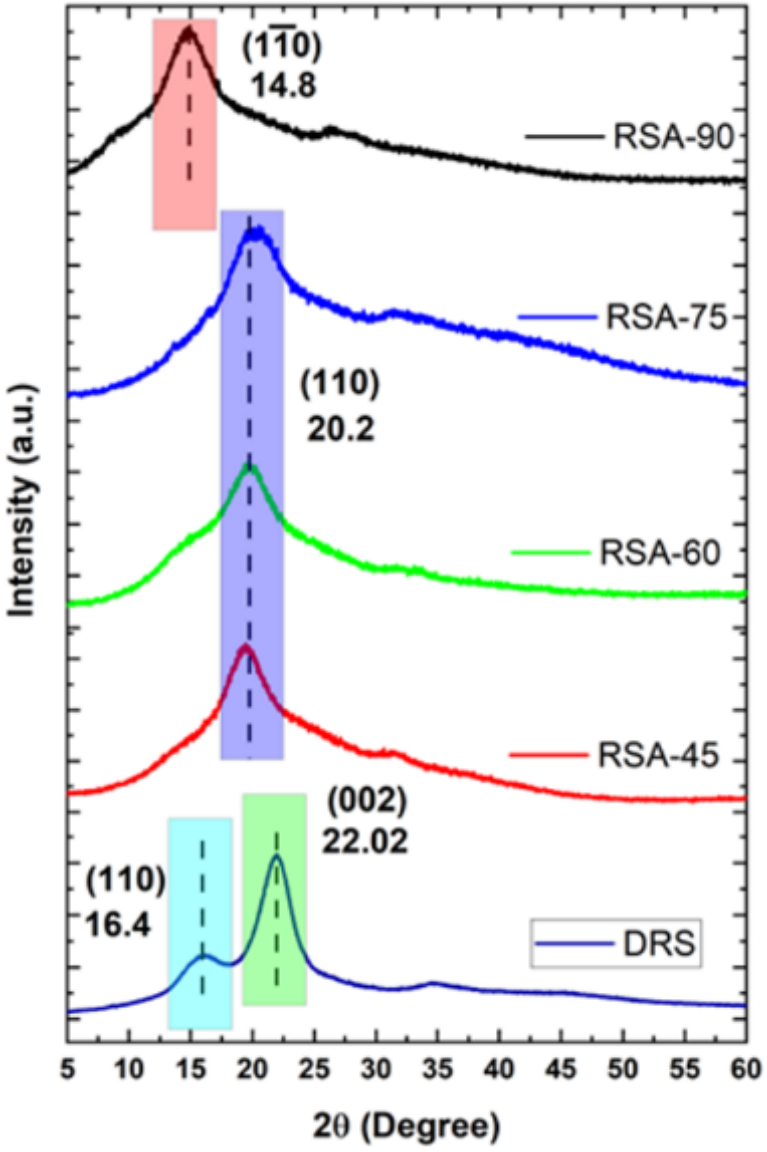

Figure 6.19 *XRD spectra of delignified rice straws and phosphorylated samples at different curing times*

6.3.7 Flammability test of RSA and RS thermal box

The combustion test of RSA-45 (experimental setup shown in ***Figure 6.20*****(a)**) was performed to investigate its stability under direct exposure to flame and its utilisation as flame retardant material. As shown in ***Figure 6.20*****(b)**, the test was

performed for 86 seconds, and it was observed that the colour of the top portion of the RSA-45 remained white, which demonstrated its thermal stability as the flame could not penetrate aerogel. The char generated after the combustion was 53.13 ± 1.9%, and the combustion rate was 0.04 cm/second. The lower weight reduction (46.8% char) and a slower combustion rate in the RSA-45 were possibly due to the grafting of phosphate groups and inherent silica in the cellulose structure (rice straw, ***Figure 6.20*****(b)**). Early combustion of aerogel might be due to the catalytic action of grafted phosphate ions responsible for dehydration and resulted in generating many non-combustible gases, effectively absorbing the heat and reducing the concentration of combustible gases. The presence of polyphosphate in the combustion process of RSA-45 aerogel was found to improve the thermal degradation of cellulose, resulting in increased production of polyaromatic char at elevated temperatures [17]. As shown in ***Figure 6.20*****(c)**, the direct combustion of the developed box (RSA-45) does not catch fire in the whole experiment without any deformation in its original shape. However, the box made from polystyrene was deformed entirely, melted, and lost its original structural integrity under the same experiment condition.

6.3.8 Morphological properties of RSA

The effect of phosphorylation and homogenisation processes on the morphological properties of the developed aerogels RSA-45, RSA-60, RSA-75, and RSA-90 are shown in ***Figure 6.21*****(a-i).** As observed in the ***Figure 6.21***, a large porous structure of cellulose fibres (32.2 µm average pore size, ***Figure 6.21*****(m)**) with stacked leafy morphology can be seen in all the developed aerogels, which is possibly due to the sublimation of the frozen water molecules during the freeze drying. The intertwist or crumbling of cellulose fibres fibre structure might be due to the homogenisation and casting of gel followed by freeze-drying. The presence of silica was also observed in

the developed aerogels with an average diameter of 3.6µm (***Figure 6.21*(n)**)) which helped in proving the water stability of the aerogels. Elemental mapping and EDAX analysis of the developed aerogels are presented in ***Figure 6.21*(j-l)**. The presence of phosphate groups in the cellulose structure confirms the evidence of phosphorylation process, and the persistence of silica even after phosphorylation confirms its existence in the rice straws.

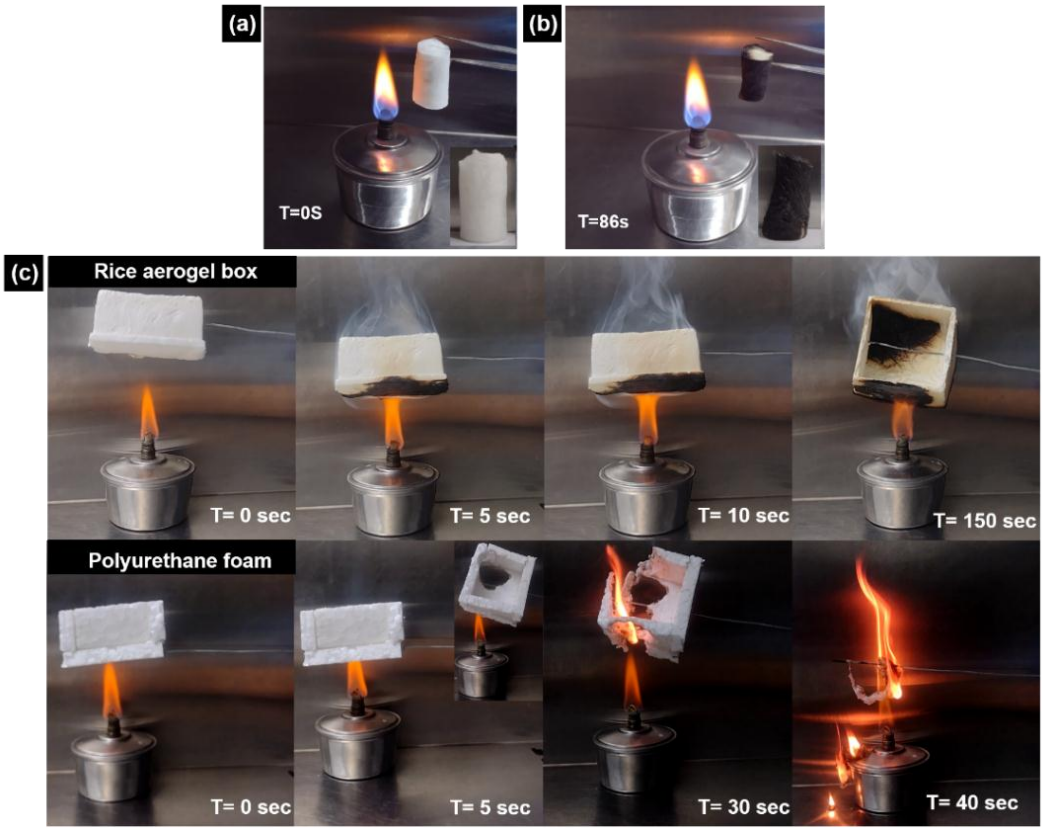

Figure 6.20 *(a) Flammability test of RSA-45 at t=0 sec, (b) flammability test of RSA-45 after 86 sec, (c) the effect of direct flame on the RSA-45 box and polyurethane box.*

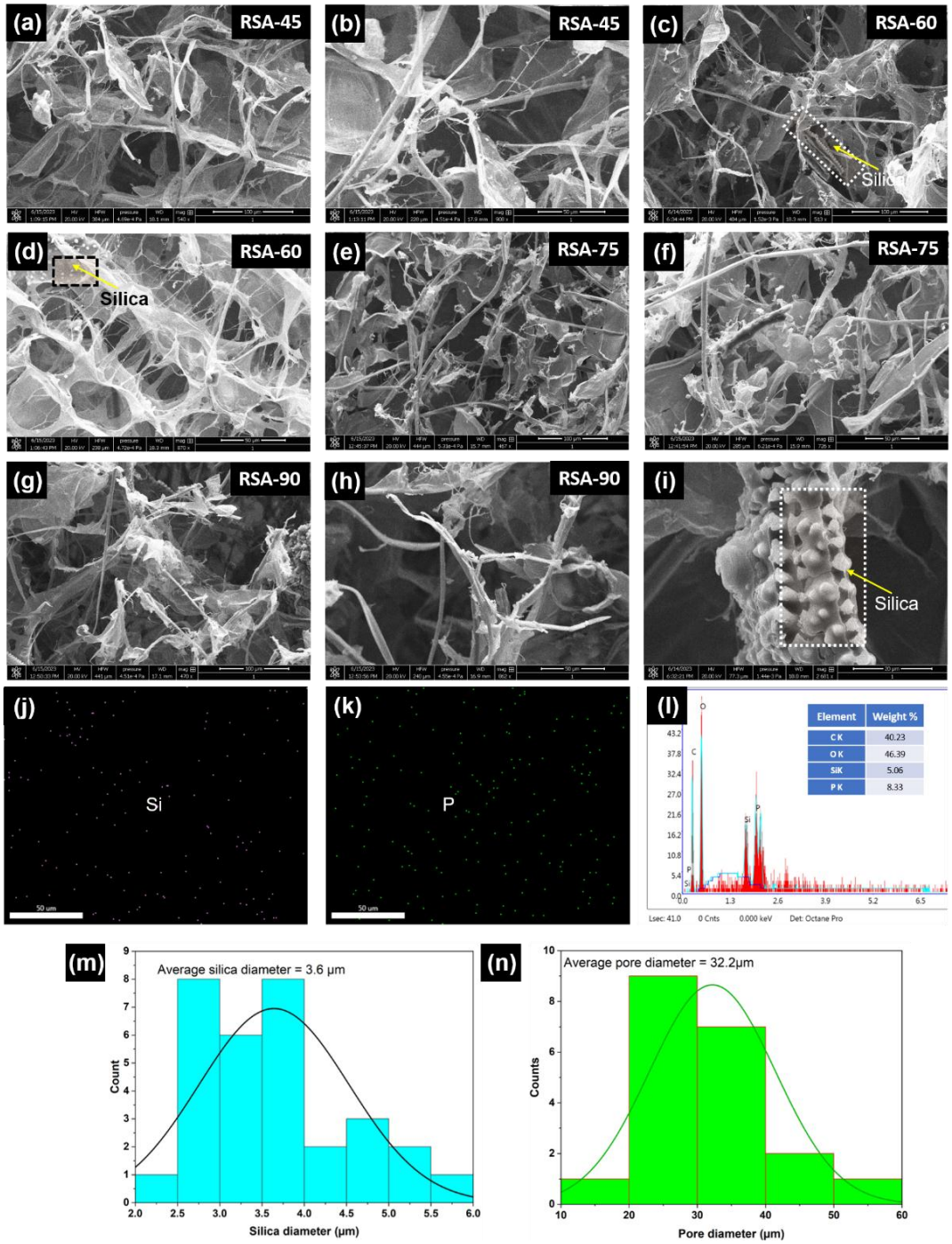

Figure 6.21 *SEM micrograph of aerogels produced at different curing time (a-i), presence of silica on the aerogel fibres, (i) elemental mapping of elements (j) Si, (k) P, and (l) EDS spectrum of RSA-60 with elemental weight percent, (m) silica average diameter, and (n) average pore size of aerogels.*

6.3.9 Melting behavior and IR imaging of the butter

The melting behaviour of the butter at different intervals of time was checked, and photographs were taken using a camera and thermal imager, as depicted in ***Figure 6.22*****(a)**. Initially, butter was taken out from -20 °C. However, the temperature of the butter increased to -2 °C when the experiment started at T = 0 minute for the butter kept in a plastic package and -10 °C for the butter kept inside the RSA-60 box. The shape of the butter was intact and uniform and maintained its original chromosomal shape with no melting behaviour until the end of 120 minutes for both cases. During the 180-240 minutes of incubation, the shape of the butter started to deform, and initiation of melting was observed in the case of butter kept in a plastic box. The butter completely melted, and structural integrity was lost between 240-360 minutes in the case of plastic packaging. However, no change in the shape of the butter and melting initiation was observed for the case in which butter was packed in the RSA-60aerogel boxes. These results confirm that the developed box can be used to preserve butter for a longer time without melting. The significant temperature difference between the aerogel box and the surrounding environment can be attributed to the unique properties of RSA aerogel (***Figure 6.22*** **(b)**), such as its low thermal conductivity and high porosity.

6.3.10 Packaging of butter in RS box

The developed RSA-45 box was utilised for the butter packaging to study the physical, chemical, and microbiological changes over different preservation periods and temperatures. ***Figure 6.23*** shows that no colour changes were observed in the butter samples incubated at 4 °C for 0 and 7 days. However, the butter turns to slight yellows when incubated at 25 °C in the control condition, and initiation of melting was also observed at 25 °C in the butter sample after incubation of 7 days.

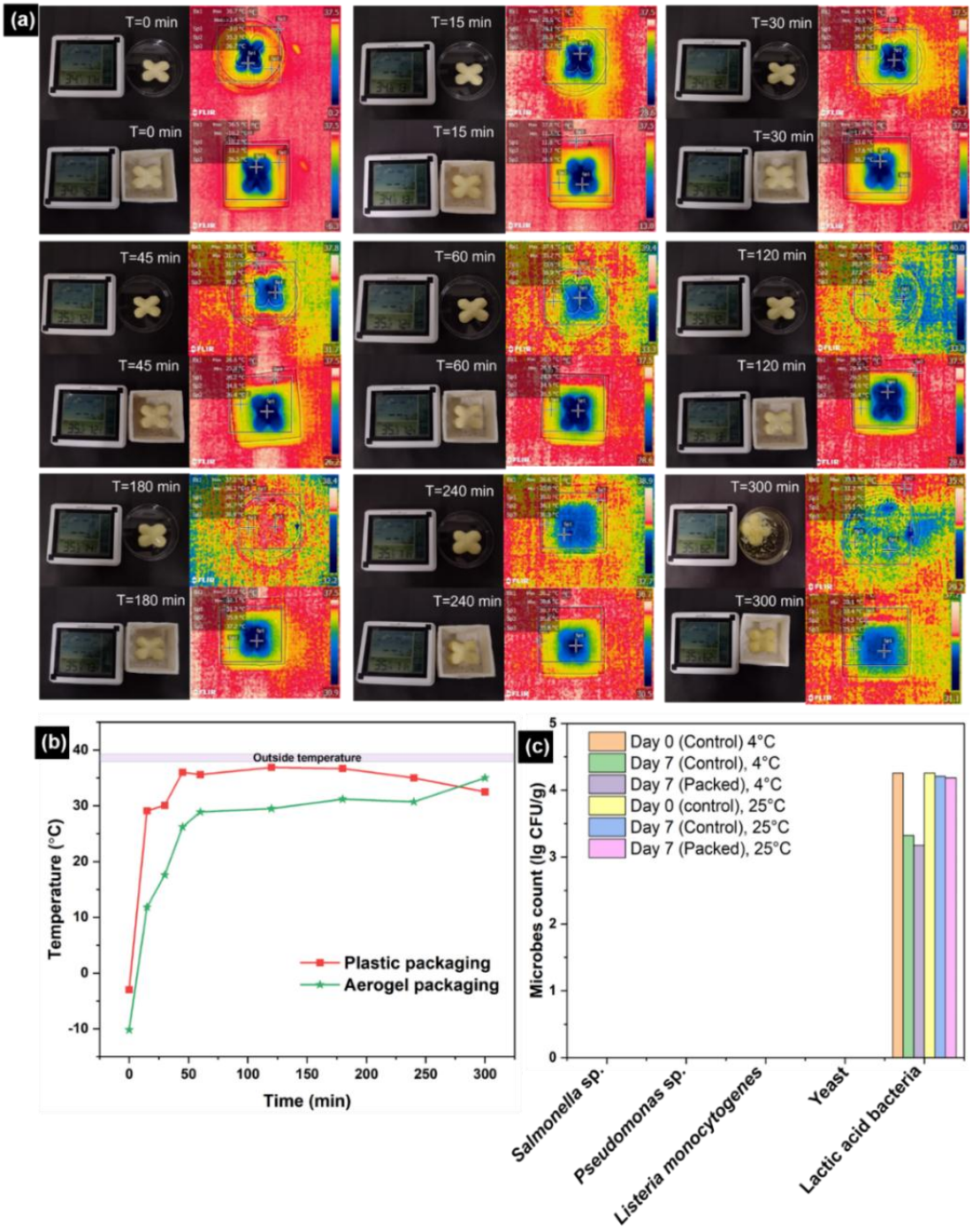

Figure 6.22 *(a) Melting behaviour of the butter at different intervals of time in packaged aerogel box and unpacked condition at room temperature,(b) temperature variation in temperature of stored butter in aerogel boxes, and (c) microbiological study of the stored butter at 4 and 25 °C under control and packed conditions t understand the effect of incubation period on growth of pathogenic bacteria such as Salmonella species, Pseudomonas species, Listeria monocytogenes, Lactic acid bacteria and yeast count.*

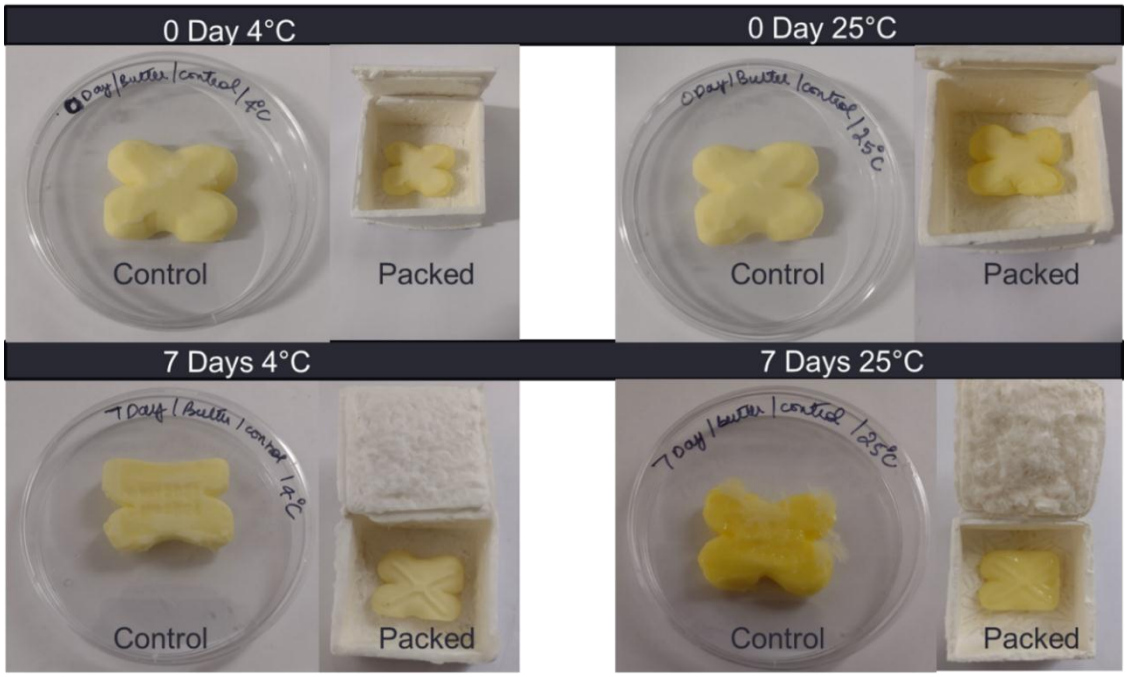

Figure 6.23 *Photographs of the butter (packed and controlled) at 4 °C and 25 °C stored for 0 and 7 days.*

As shown in ***Table 6.5***, a slight decrease in the pH of butter was observed during the storage period of 7 days at 4 °C and 25 °C in both packed and control samples. Overall, the peroxide values increased during the storage period in both the control and packaging of the butter. The maximum increase in butter's peroxide values and pH were observed at 25 °C due to an increased temperature, accelerating the oxidative rancidity in control samples stored at 4°*C* and 25 °C. A slight increase in the peroxide value of butter was observed in the packed condition at both storage temperatures 4 °C and 25 °C on day 7.

Table 6.5 *Changes in pH and peroxide values over a 7-day storage period under the control and packaged conditions at 4 °C and 25 °C.*

Condition	Day 0 4 °C	Day 0 25 °C	Day 7 4 °C	Day 7 25 °C
Control (Peroxide value), mmol/kg	1.71	1.76	1.93	2.18
Control (pH value)	6.23	6.20	6.23	6.15
Packed (Peroxide value), mmol/kg	1.71	1.73	1.72	2.15
Packed (pH value)	6.21	6.23	6.21	6.18

From the graph, microbiological analysis of the butter samples was also performed to study the growth of different food pathogens on stored butter samples in selective media such as XLD agar, *Pseudomonas* agar, PALCAM agar, PDA agar, and MRS agar to evaluate the growth of *Salmonella species, Pseudomonas species, Listeria monocytogenes*, yeast and Lactic acid bacteria respectively. As shown in ***Figure 6.24***, growth of *Salmonella* species, *Pseudomonas* species, and *Listeria monocytogenes* were not observed in any XLD agar plates, *Pseudomonas* agar plate and PALCAM agar plate incubated at 4°C and 25 °C in both packed and control sample indicating that the developed packaging box can prevent the growth of pathogenic bacteria over the storage period of 0-7 days. No growth of yeasts was observed in the samples stored at 4°C and 25 °C in packed condition on day 0. However, a slight increase in yeast growth was observed at 4°C and 25 °C and was 1.4 and 1.9 log CFU/g of butter, respectively. The lactic acid bacterial load was increased over the 0-7 days incubation at both 4°C and 25 °C. At day 0, the total lactic acid bacteria counts were 4.225 log CFU/g at both incubated temperatures. The lactic acid bacterial load on day 7 incubated at 4 °C was 3.322 and 3.176 log CFU/g for control and packed butter samples. For the sample incubated at 25 °C, the bacterial load increased to 4.204 and 4.181 log CFU/g for control and packed butter samples after seven days of storage (***Figure 6.22*** (c)). These studies

suggest that the synthesised RSA-45 aerogel boxes can effectively preserve butter for seven days.

6.3.11 LCA of storage of butter in RSA and plastic boxes

LCA was conducted to assess the environmental impacts associated with the production process and storage durations of butter packaging, comparing plastic and aerogel boxes (***Figure 6.25*****(a-c)**). The most significant environmental impacts occurred in three distinct categories during the production and storage of butter in plastic boxes. These categories include climate change (both with and without biogenic carbon considerations), terrestrial ecotoxicity, and fossil depletion, resulting in impact values of 25 kg CO_2 eq., 23.3 kg 1,4-DB eq., and 7.57 kg oil eq. respectively. The increased environmental impact values observed in the PET packaging system can be primarily attributed to the greater use of electricity-intensive methods in producing PET resin and the thermoforming process. In contrast, the aerogel packaging system exhibits the highest impact value of 21.8 kg CO_2 eq., 2.11 kg 1,4-DB eq., and 4.78 kg oil eq. for climate change (both with and without biogenic carbon considerations), terrestrial ecotoxicity, and fossil depletion respectively. These impact values were mainly due to the energy-intensive processes during aerogel production. Compared to the plastic packaging system, the reduced environmental impact values associated with the aerogel packaging system can primarily be attributed to refrigerating the butter for 6 hours to preserve its structure and prevent melting in the plastic packaging. However, in the case of aerogel packaging, its low thermal conductivity prevents butter from melting, eliminating the need for a refrigeration system and consequently resulting in lower impact values.

6.3.11.1 Normalization of mid-point results from storage of butter in RSA and plastic boxes

Normalising the impact values generated upon butter storage inside the PET box (***Figure 6.25*(e)**) was performed to observe the dominant categories. Fossil depletion, photochemical ozone formation and terrestrial acidification were observed to be the dominant categories, with values of 0.0078 kg oil eq, 0.0053 kg NO_x eq and 0.0037 kg SO_2 eq., respectively. The significant impact in this category occurs due to the electricity consumption during PET production and subsequent butter storage. Since butter storage uses electricity during preservation, the dominant category doesn't change and displays increased values. The butter stored in rice aerogel boxes don't consume electricity; therefore, changes in the values during normalisation were not observed (similar to rice aerogel production, ***Figure 6.25*(d)**).

6.3.11.2 Sensitivity analysis of storage of butter in RSA and plastic boxes

The sensitivity analysis was performed to observe the changes in impact values of various processes, such as electricity production, TPA production and PET resin production, during PET box production on the values dominant impact categories ***Table 6.6***. With a 10 % increase in electricity, fossil depletion, photochemical ozone formation, and terrestrial acidification display an increase of 6.74 %, 10.06 %, and 9.80 %, where a decrease in electricity value by 8% results in a reduction of impacts by 5.28 %, 7.78 % and 7.82 %.

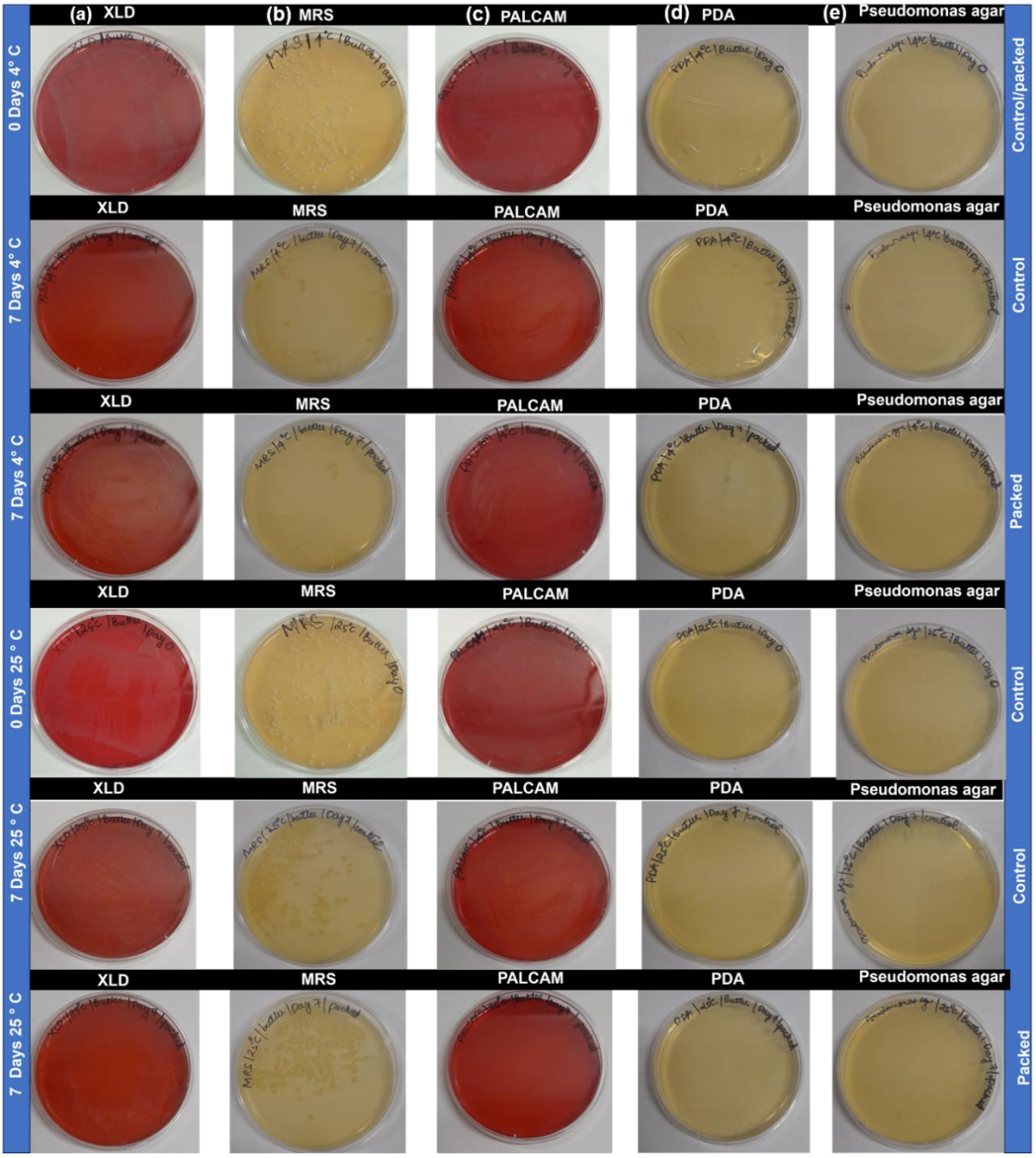

Figure 6.24 *Photograph of the different selective plates to study the growth of different pathogenic microorganisms such as (a) XLD (Salmonella species), (b) MRS (Lactic acid bacteria), (c) PALCAM (Listeria monocytogenes) (d) PDA (yeast) and (e)Pseudomonas agar (Pseudomonas species) in stored butter samples at 4 and 25 °C under control and packed conditions.*

Table 6.6 *Sensitivity analysis of the dominant environmental categories for producing PET boxes and their utilisation for butter storage under refrigeration system.*

Categories	**Electricity**		**TPA production**		**PET resin**	
	10% increase	8% decrease	10% increase	8% Decrease	10% increase	8% decrease
Fossil depletion	6.74	-5.28	0.26	-0.13	4.36	-3.30
Photochemical Ozone formation	10.06	-7.76	0.21	-0.21	4.82	-4.93
Terrestrial **a**cidification	9.80	-7.84	0.00	0.00	5.88	-5.23

TPA production with a 10% increase in the input value results in 0.26%, 0.21% and 0% increases in fossil depletion, photochemical ozone formation and terrestrial acidification impact categories, whereas PET resin shows 4.36%, 4.82% and 5.88% increase in these categories. A reduction of input quantities by 8% during TPA production results in 0.13%, 0.21% and 0% decrease in impact value for fossil depletion, photochemical ozone formation and terrestrial acidification. In contrast, for PET resin with an 8% reduction in input, 3.3%, 4.9% and 5.23% decreases in impact values were observed. This suggests that PET box utilisation for butter storage is controlled by electricity, PET resin, and TPA production. ***Table 6.7*** shows three categories, fossil depletion, photochemical ozone formation and terrestrial acidification, chosen as dominant categories to study their changes in the input values of processes involved, such as electricity, delignification, and phosphorylation. A 10% increase in the input values of electricity resulted in 10.09%, 10.04% and 9.73% increased impact values under fossil depletion, photochemical ozone formation and terrestrial acidification categories, respectively. An 8% decrease in the input values of electricity results in -7.8. -7.95 and -7.96 decrease in the impact values under fossil

depletion, photochemical ozone formation and terrestrial acidification categories, respectively.

Table 6.7 *Sensitivity analysis of the dominant environmental categories for producing rice aerogel boxes and their utilisation for butter storage.*

Categories	**Electricity**		**Delignification**		**Phosphorylation**	
	10% increase	8% decrease	10% increase	8% decrease	10% increase	8% decrease
Climate change (Including biogenic carbon)	10.09	-7.80	5.05	-3.67	3.21	-2.75
Climate change (Excluding biogenic carbon)	10.09	-7.80	5.05	-3.67	3.21	-2.75
Fossil Depletion	10.04	-7.95	4.81	-3.97	3.35	-2.72
Photochemical Ozone formation	9.73	-7.96	4.72	-4.13	3.24	-2.65

Furthermore, a 10% decrease in the input values of the delignification process increased by 5.05%, 4.81% and 4.72% impact values of fossil depletion, photochemical ozone formation and terrestrial acidification categories, respectively. An 8% decrease in the input values resulted in -3.67%, -3.97% and -4.13% decrease in the impact of fossil depletion, photochemical ozone formation and terrestrial acidification categories, respectively. Additionally, a 10% increase in the input values of the phosphorylation process resulted in a 3.21%, 3.35% and 3.24% increase in the fossil depletion, photochemical ozone formation and terrestrial acidification categories, respectively. However, an 8% decrease in the input values resulted in -2.75%, -2.72% and -2.65% decrease in the impact values of fossil depletion, photochemical ozone formation and terrestrial acidification categories. This finding suggests that changes in the input values of the processes involved during butter storage in PET boxes and rice aerogel boxes significantly affected the overall impact values.

6.3.12 LCA of RS and plastic boxes production for the transportation of butter under a cold storage system

LCA was performed to evaluate the effects of the transportation of butter from the production plant to the retailer shop under a cold storage system. As shown in ***Figure 6.26*****(a-c)**, the maximum impact value was generated in climate change, default, excl biogenic carbon and fossil depletion category during the transportation of butter under cold storage conditions for both rice aerogel box and PET box with the maximum values of 31 and 30.3kg CO_2 eq. and 22.5 and 21.8 kg oil eq. respectively. The impact values generated in terrestrial ecotoxicity and human toxicity, non-cancer category were 6.45 and 24.5 kg 1,4-DB eq. and 2.38 and 4.31 kg 1,4-DB eq. respectively, for both cases. The lower terrestrial ecotoxicity values for the transportation of butter in rice aerogel boxes under cold storage were mainly due to the utilisation of electricity, diesel consumption and *p*-xylene production.

6.3.12.1 Normalization of mid-point results of transportation of butter in RSA and plastic boxes under cold storage conditions

The normalisation of impact values derived from the transportation and cold storage of butter in PET boxes (***Figure 6.26*****(d)**) and rice aerogel boxes (***Figure 6.26*****(e)**) was conducted to identify the primary impact categories. The study revealed that the most significant categories were fossil depletion, climate change, and photochemical ozone formation, with corresponding values of 0.022, 0.0038, and 0.0032, respectively, for transportation of butter under cold storage conditions in PET boxes, while in the rice aerogel boxes, it was 0.022, 0.0059 and 0.0042 for fossil depletion, photochemical ozone formation and terrestrial acidification respectively. The utilisation of electricity during the production of boxes and diesels during the transportation of butter in cold

storage results in ongoing energy consumption, leading to the consistent dominance of categories mentioned above with progressively higher values. Nevertheless, employing rice aerogel boxes for butter packaging and transportation resulted in lower values for normalising midpoint results.

6.3.12.2 Sensitivity analysis of the transportation of butter in RSA and plastic boxes under cold storage conditions

A sensitivity analysis was conducted to assess the influence of different processes associated with the transportation of butter in PET boxes under cold storage conditions on key environmental impact categories, namely electricity production, extrusion, and transportation, shown in ***Table 6.8***. The studies conducted in this study revealed a positive correlation between a 10 % rise in electricity production derived from fossil fuels and subsequent increases of 1.83 % in fossil depletion, 7.62 % in photochemical ozone formation, and 7.95 % in terrestrial acidification. In contrast, a reduction of 8% in electricity consumption led to corresponding decreases of -1.83 %, -6.38 %, and -5.68 % in fossil depletion, photochemical ozone formation, and terrestrial acidification, respectively. Similarly, it was noted that an increase of 10 % in input values of extrusion processing resulted in increases of 0.0 %, 0.95 %, and 1.14 % in the impacts of fossil depletion, photochemical ozone formation, and terrestrial acidification, respectively. Conversely, when the input values are reduced by 8%, the impact values for fossil depletion, photochemical ozone formation, and terrestrial acidification decrease by -0.46 %, -0.95 %, and -0.57 %, respectively. Additionally, it was observed that there was a 10 % increase in the input values of transportation, resulting in increases of 6.88 %, 1.09 %, and 2.27 % in the impact values under the categories of fossil depletion, photochemical ozone formation, and terrestrial

acidification, respectively. A reduction of 8% in the input values resulted in decreases of -5.50 %, -1.90 %, and -1.70 % in fossil depletion, photochemical ozone formation, and terrestrial acidification, respectively. This implies that the environmental impacts of PET boxes used for transportation under cold storage conditions are significantly influenced by electricity consumption, extrusion, and transportation production.

Table 6.8 *Sensitivity analysis of the dominant environmental categories for transportation of butter in RS aerogel boxes.*

Categories	**Electricity**		**Lyophilisation**		**Transportation**	
	10% increase	8% decrease	10% increase	8% decrease	10% increase	8% decrease
Climate change (including biogenic carbon)	6.77	-5.81	0.97	-0.97	2.90	-2.58
Climate change (excluding biogenic carbon)	7.10	-5.48	1.29	-0.97	3.23	-2.26
Fossil depletion	1.78	-1.78	0.44	-0.44	8.00	-6.22
Photochemical Ozone formation	5.98	-4.75	1.05	-0.70	4.04	-3.34

A sensitivity analysis was conducted to assess the variations in the impact values associated with the transportation of butter in rice aerogel boxes (***Table 6.9***), specifically in the absence of cold storage conditions. This study evaluated changes by examining three processes: electricity, lyophilisation, and transportation. A 10% increase in the input electricity values led to corresponding increases of 6.77%, 1.78%, and 5.98% in the impact values under the categories of climate change, fossil depletion, and photochemical ozone formation, respectively. Conversely, an 8% decrease in the input electricity values resulted in a reduction of -5.81%, -1.78%, and -4.75% in the impact values on climate change, fossil depletion, and photochemical ozone formation categories, respectively. In addition, it was observed that a 10% increment in the input

values of the lyophilisation process led to corresponding increases of 0.97%, -0.44%, and 1.05% in the impact values associated with climate change, fossil depletion, and photochemical ozone formation categories, respectively. A decrease of 8% in the input values led to corresponding reductions of -0.97%, -0.44%, and -0.70% in the impact values for climate change, fossil depletion, and photochemical ozone formation, respectively. Furthermore, a reduction of 10% in the input values of transportation led to an increase in impact values of 2.9%, 8.0%, and 4.04% in the categories of climate change, fossil depletion, and photochemical ozone formation. Similarly, a decrease of 8% resulted in impact values of -2.58%, -6.22%, and -3.34% in the same categories.

Table 6.9 *Sensitivity analysis of the dominant environmental categories for transportation of butter in PET boxes.*

Categories	**Electricity**		**Extrusion**		**Transportation**	
	10% increase	8% decrease	10% increase	8% decrease	10% increase	8% decrease
Fossil Depletion	1.83	-1.83	0.00	-0.46	6.88	-5.50
Photochemical Ozone formation, Eco	7.62	-6.38	0.95	-0.95	1.90	-1.90
Photochemical Ozone formation, HH.	7.69	-6.73	0.96	-0.96	0.96	-1.92
Terrestrial acidification	7.95	-5.68	1.14	-0.57	2.27	-1.70

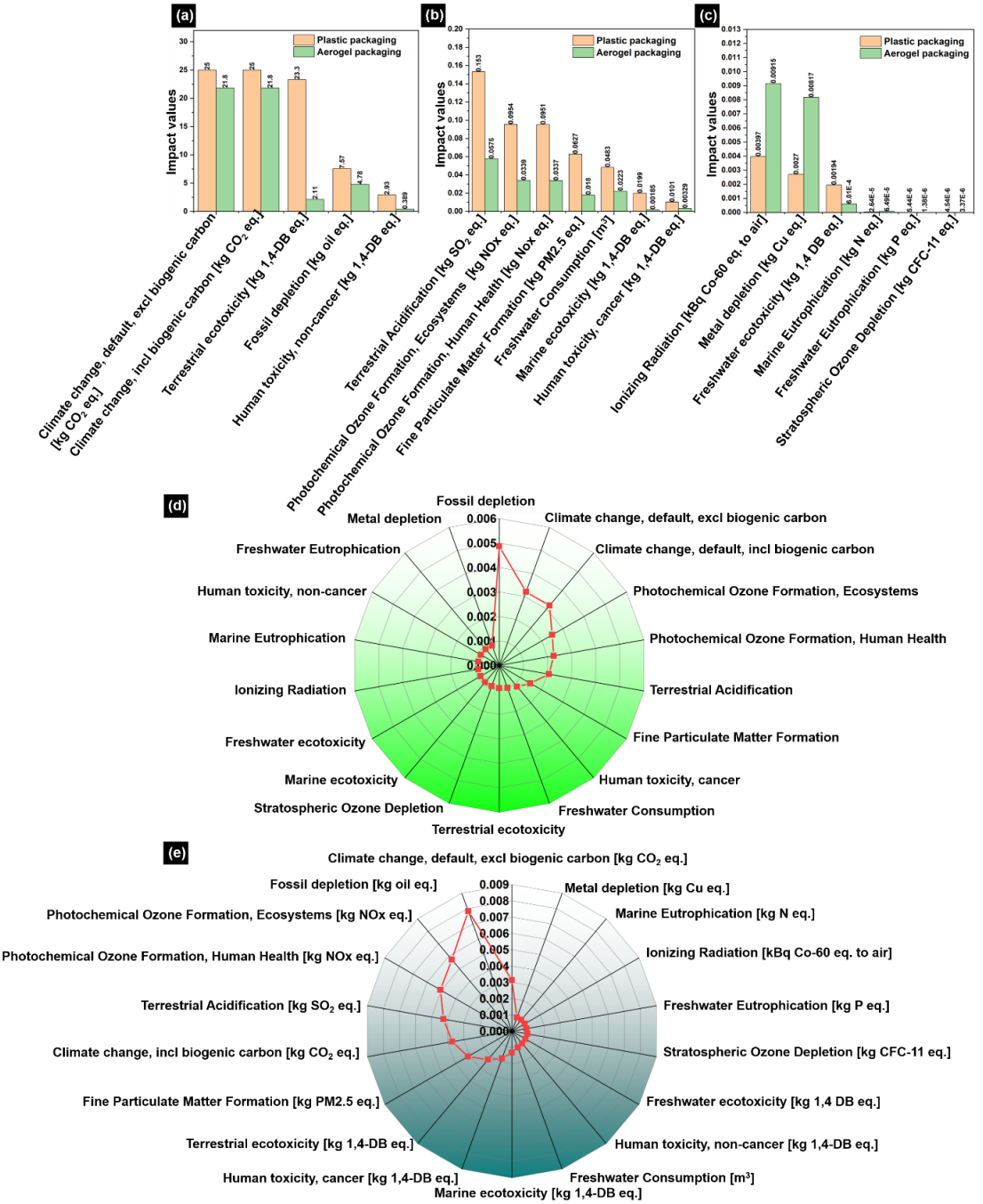

Figure 6.25 *(a-c) Mid-point impacts values generated during the storage of butter in rice aerogel box and PET box production, (d) normalisation of mid-point results from rice aerogel box production and (e) PET box production.*

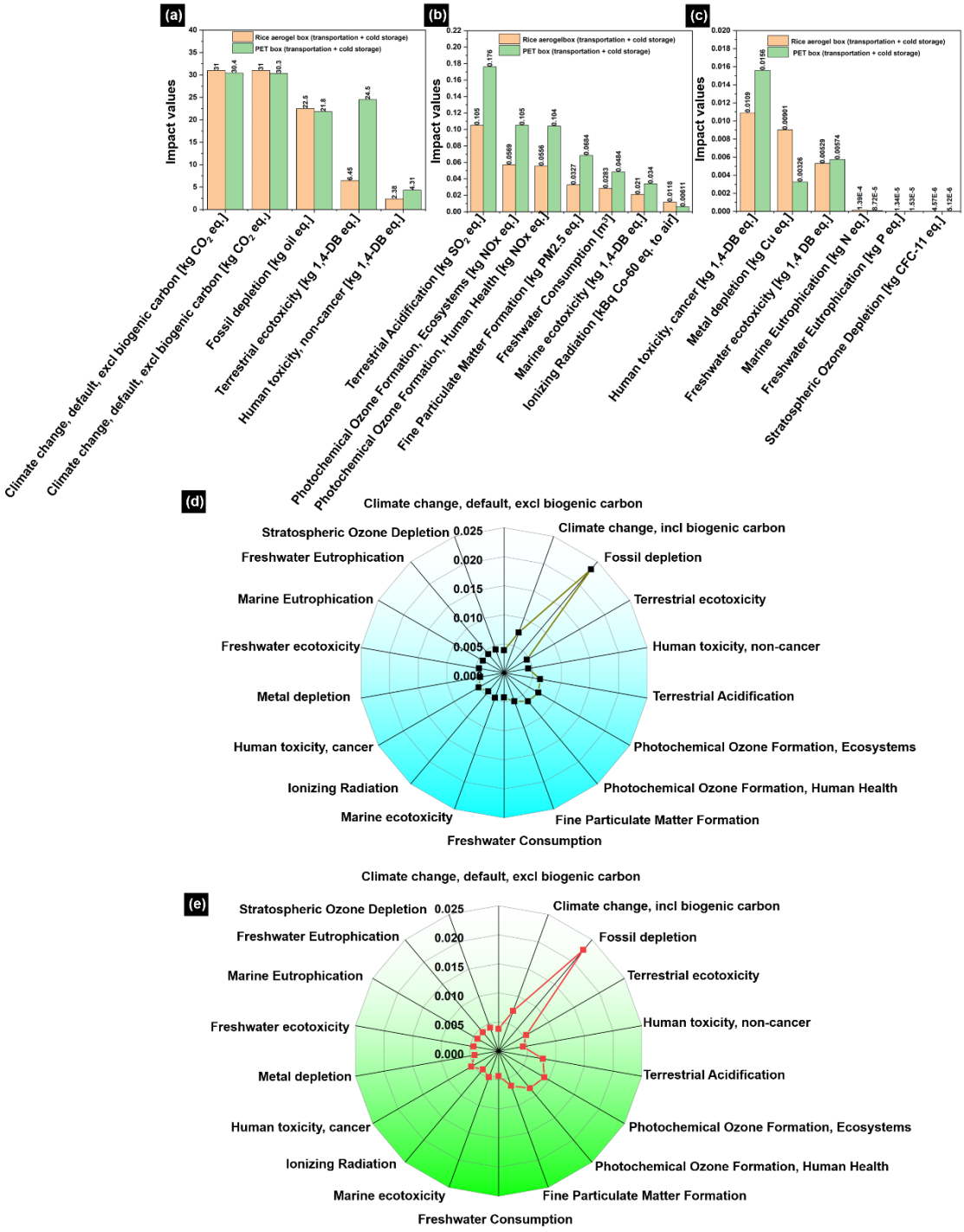

Figure 6.26 *(a-c) Mid-point impacts values generated during the transportation and cold storage of rice aerogel box and PET box production, (d) normalisation of mid-point results from rice aerogel box and (e) PET box.*

6.4 Summary

In conclusion, this thesis chapter presents two innovative approaches for valorising rice straw waste, addressing significant environmental challenges associated with its disposal. The first approach involves the strategic functionalization of rice straws through delignification-*cum*-phosphorylation, resulting in the development of phosphorylated rice straw films (RSF) and moulded beverage cups. These RSFs exhibit enhanced mechanical strength, thermal stability, and flame retardancy, making them ideal for packaging applications. Moreover, the ability of all-cellulose films to be heat-sealed improves the shelf-life of perishable goods, contributing to sustainability in food preservation. Additionally, moulded cups demonstrate high solvothermal stability and improved washability post-consumption, enhancing their reusability. The second approach introduces a novel methodology for producing aerogels and aerogel boxes derived from rice straw, showcasing exceptional attributes such as lightness, low density, high porosity, and flame retardancy. These aerogels are utilized to create boxes for storing butter, demonstrating superior performance in maintaining butter (perishable and heat-sensitive) integrity without the proliferation of pathogenic microorganisms compared to conventional options. Life cycle analysis (LCA) reveals that rice aerogel boxes significantly reduce carbon emissions compared to polyurethane foam and PET boxes, particularly during storage and transportation, due to their low thermal conductivity and lack of need for refrigeration. Rice straw valorization into packaging films, drinking cups, and aerogel boxes offers a sustainable alternative to plastic-based products, offering a plastic-free the world. These innovative solutions reduce carbon emissions from perishable goods storage, transit, and cold storage, making them financially viable for a more sustainable future.